Rotary Bend Fatigue of Nitinol to One Billion Cycles

J. D. Weaver[1], **G. M. Sena**[1], **K. I. Aycock**[1], **A. Roiko**[2], **W. M. Falk**[2], **S. Sivan**[1], **B. T. Berg**[3]

[1]U.S. Food and Drug Administration (FDA), Silver Spring, MD, USA

[2]Medtronic, Mounds View, MN, USA

[3]Boston Scientific (BSC), Maple Grove, MN, USA

Abstract

Nitinol implants, especially those used in cardiovascular applications, are typically expected to remain durable beyond 10^8 cycles, yet literature on ultra-high cycle fatigue of nitinol remains relatively scarce and its mechanisms not well understood. To investigate nitinol fatigue behavior in this domain, we conducted a multifaceted evaluation of nitinol wire subjected to rotary bend fatigue that included detailed material characterization and finite element analysis as well as post hoc analyses of the resulting fatigue life data. Below approximately 10^5 cycles, cyclic phase transformation, as predicted by computational simulations, was associated with fatigue failure. Between 10^5 and 10^8 cycles, fractures were relatively infrequent. Beyond 10^8 cycles, fatigue fractures were relatively common depending on the load level and other factors including the size of non-metallic inclusions present and the number of loading cycles. Given observations of both low cycle and ultra-high cycle fatigue fractures, a two-failure model may be more appropriate than the standard Coffin-Manson equation for characterizing nitinol fatigue life beyond 10^8 cycles. This work provides the first documented fatigue study of medical grade nitinol to 10^9 cycles, and the observations and insights described will be of value as design engineers seek to improve durability for future nitinol implants.

Keywords

Fatigue; NiTi materials; Mechanical behavior

Introduction

Fatigue of nitinol, the nearly equiatomic alloy of nickel and titanium, has been a topic of interest to researchers for many years given its unique thermomechanical properties and applications. Several in-depth reviews have provided thorough discussions of the many factors affecting nitinol fatigue [1–5]. As the use of nitinol in implantable medical devices

has grown over the years and expectations regarding implant durability have risen, interest in ultra-high cycle fatigue (UHCF) of nitinol has likewise increased [6]. Unfortunately, much of the research on nitinol fatigue has been restricted to runout cycle counts of 10^6 or 10^7 cycles [7–12] which is well below the approximate 4×10^8 cycle count associated with 10 years of cardiac loading [13]. Some recent research on nitinol fatigue has extended beyond 10^7 cycles with several studies extending to runout cycle counts of 10^8 [14–18]. To date, however, only two studies have published fatigue data beyond 10^8 cycles, although neither conducted experiments to runout at 10^9 cycles [19, 20]. Of note, nitinol fatigue tests are routinely conducted to 4×10^8 or 6×10^8 cycles as part of pre-clinical testing that is included in medical device regulatory submissions, but such studies are meant to demonstrate implant safety and performance and are thus not published in the open literature. In general, there is a lack of knowledge of nitinol fatigue mechanisms in UHCF, especially in the open literature.

UHCF of more conventional materials has been studied using both traditional, low frequency, tests, and ultrasonic methods. Translating the ultrasonic methodology to nitinol specimens has been difficult and thus far no exhaustive study of nitinol fatigue with ultrasonic methods has been completed [6]. Such studies of UHCF, regardless of the test frequency, are important because unique fatigue crack initiation mechanisms may occur in UHCF. UHCF crack initiation in stainless steel, for example, may occur at internal locations and result in a 'fisheye' appearance of the fracture surface [21, 22].

Urbano et al. used fracture mechanics to analyze the inclusions or defects that caused fatigue failure in nitinol [17]. Their approach combined the loading and the size of the inclusion to predict the fatigue strength. This approach is commonly used in steels and other metals and can be a powerful tool to understand the local failure mechanisms that are driving fatigue failure [23]. Given the importance of UHCF to long-term durability of nitinol implants and the lack of published data, it is critical to study nitinol fatigue and understand its mechanisms in the UHCF domain. Thus, for the present study, we use a multifaceted approach to fatigue testing centered on rotary bend fatigue testing of straight nitinol wire specimens which additionally includes extensive metallography and material characterization, full three-dimensional finite element analysis (FEA) of our specific experimental setup, statistical modeling of the fatigue data, and a strain intensity analysis based on inclusion measurements of fatigue fracture surfaces. Because both the statistical modeling and strain intensity analysis were developed after obtaining the experimental fatigue results, those sections are each presented separately as a part of "Discussion" section.

Materials and Methods

To facilitate repeatability and reproducibility of our results as well as comparison of the performance of other materials to that of the specific nitinol alloy considered herein, we have provided a thorough description of our experimental specimens including raw material characteristics, processing parameters, and material characterization as follows.

Nitinol Wire Processing

The raw starting material was a spool of 0.508 mm diameter wire from Fort Wayne Metals NiTi #1, lot 10,796,614, purchased March 2017. The material's ingot A_s, A_{peak}, A_f is {− 26, − 16, − 10} °C. Composition as assessed by ASTM F2063-12 [24] is: Ni 56.2%, O 0.023%, Fe 0.018%, C 0.003%, Cr ˂ 0.005%, Co ˂ 0.005%, Cu ˂ 0.005%, H ˂ 0.001%, Nb ˂ 0.01%, with the remainder Ti. The wire as manufactured was cold worked to have a 46.2% cross-sectional area reduction. It was provided in the straightened annealed condition, dark oxide, with an active A_f of 3 °C as determined by ASTM F2082-16 [25]. Tensile properties of unprocessed wires measured per ASTM F2516-18 [26] at 22 ± 2 °C are as follows: ultimate strength of 1512 MPa, upper plateau of 556 MPa, lower plateau of 201 MPa, and permanent set of 0.04%.

The wires were heat treated for 10 min in a 515 °C fluidized aluminum oxide bath followed by a water quench. The wires were micro-blasted with aluminum oxide to remove surface oxides. Electropolishing removed approximately 6% of the mass resulting in wire diameters between 0.4923 and 0.4826 mm measured using a laser micrometer. Individual wires' diameters were measured to facilitate calculation of specimen-specific bending strains.

Differential Scanning Calorimetry (DSC)

For measuring the zero stress phase transformation temperatures and enthalpies, DSC was used per ASTM F2004-17 [27]. Specifically, a short segment of a wire specimen was cut using an aluminum oxide abrasive saw (Mark V PCS-400) with coolant. The specimen was weighed and placed in an aluminum sample pan with a lid. With an identical empty reference pan, the pans were placed in the TA Instruments DSC, model Q2000 with Liquid Nitrogen Cooling System. The pans were then preheated to 125 °C. While carefully recording the power differential, the pans were then cooled to − 175 °C and subsequently heated to 125 °C at a rate of 10 °C/min. On completion of the test, the power differential versus temperature was plotted and the phase change temperatures and enthalpies measured.

Surface Roughness Measurement

Surface roughness was measured on one straight wire using a Keyence VK-X1000 Laser Microscope 3D Surface Profiler over five lengths circumferentially and three lengths longitudinally. The following results were recorded: R_a, the average of surface heights, R_z, the average maximum peak to valley, and R_{sm}, the mean width (wavelength) of profile elements.

Hardness Testing

Vickers hardness of the wire were tested on a Clark CM-700 AT Micro Hardness Tester following ASTM E384-17 [28]. As described below in "Inclusion & Grain Size Analysis" section, specimens were mounted, polished to near the midline for the longitudinal samples, and etched for the grain size test. The indenter was pressed into the surface near the middle of the cross-section with loads of 25, 50, or 100 g and held for 10 s. A linear indentation spacing of 0.5 mm was used to prevent near-field strain-hardening. The tests were performed at the lab temperature, 20 to 25 °C. Five measurements were made at each load magnitude. The length of the diagonal was measured using an optical microscope.

Tensile Testing

Tensile tests per ASTM F2516-18 [26] of two processed wires were performed on an MTS Sintech load frame in air at 37 °C using a 1 kN load cell, serrated grips with 63.5 mm separation, and a 25.4 mm gauge length extensometer with measuring range of 20% strain, MTS model 634.31E-24. The pull speed was 0.0127 mm/s. The load sequence was preload 4.45 N—zero displacement (0% strain)—pull to 6% strain—unload to 0 (force)—load to break with the upper plateau stress measured between 2.95 and 3.0% strain and the lower plateau stress measured between 2.55 and 2.45% strain. Reduction of area was measured using scanning electron microscopy (SEM).

Inclusion & Grain Size Analysis

Three wires were each divided into six segments. Then, three segments of each wire were mounted longitudinally with the other three segments of each wire were mounted transversely (Fig. 3). The epoxy-mounted samples were ground using silicon carbide papers, followed by polishing using standard metallographic techniques (ASTM E3-11 [29]); specifically, polishing was performed using 9 and 3 μm diamond polishing suspensions plus a final step using an attack polish solution consisting of 4 parts (by volume) 0.04 μm colloidal silica suspension to 1 part 30% hydrogen peroxide. All polishing steps used a Buehler AutoMet 250 Pro with opposing (contra) rotation of the head and platen to avoid directional polishing effects.

A tint etchant was used to reveal the grain structure. The specific tint etchant used (90 mL water–10 mL HCl–1 g $NH_4F \cdot HF$–28 g $K_2S_2O_5$) deposits a thin sulfide film at varying thicknesses dependent on grain orientation. Samples were immersed and polished face-up in the solution until the film developed a violet appearance visually, usually after approximately 30 to 60 s. Optical light microscopy using crossed polarized illumination produces color contrast between grains due to light interference effects with the deposited film. Images were captured at 500× and 1000× magnifications using a Leica DMi8 A metallograph (Clemex Vision PE software v8.0.485) with the drawing direction oriented horizontally in the field of view. The tint etch film was removed by re-polishing the sample with the attack polish solution. The sample was then chemically etched using 56 mL water–10 mL HNO_3–2.4 mL HF (ASTM E407-07 [30]) by swabbing with a cotton-tipped applicator until the microstructure was revealed when observing the sample through a microscope (approximately 30 s). SEM imaging was performed after chemical etching. Imaging was performed at room temperature, 22.5 ± 2.5 °C, above A_f (17.4 °C) on a Thermo-Fisher Apreo C Field Emission SEM. The heating effect of the lighting for optical microscopy was neglected.

Inclusion size (inclusion plus porosity maximum dimensions) and inclusion percent area were measured on three wires. The images were analyzed by software on 500× backscatter SEM images at a pixel resolution of 0.1993 μm. Assuming four pixels in length for resolving a particle, the minimum particle size resolved was 0.8 μm. For each wire, Boston Scientific (BSC) analyzed 9 randomly selected transverse and 9 randomly selected longitudinal sections. Each imaged area was 170 μm × 255 μm. The total area analyzed in each plane was 0.390 mm^2 per wire.

Once each specimen was measured for all resolved inclusions, the dimensions of the largest inclusion on each image were recorded. To estimate the largest transverse inclusion in a given surface area of a fatigue test specimen, the best fit Gumbel extreme value distribution

$$f(x) = \frac{1}{\delta}\left[\exp\left(-\frac{x-\lambda}{\delta}\right)\right] \times \exp\left[-\exp\left(-\frac{x-\lambda}{\delta}\right)\right] \tag{1}$$

was determined following the maximum likelihood method described in Sect. 6.9.3 of ASTM E2283-08 [31] from the distribution of the largest inclusions on the 27 individual transverse images. To calculate an expected size of inclusion in a region of high alternating strain, A_{risk}, the return period $T = A_{risk}/A_o$, where A_o, the area of each metallographic image, is determined, and the expected longest size x is calculated by

$$x = -\delta_{ML}\ln\left[-\ln\left(\frac{T-1}{T}\right)\right] + \lambda_{ML} \tag{2}$$

The standard error, SE, of the predicted longest inclusion length x was calculated using Eq. 21 in Sect. 6.9.5 of ASTM E2283-08 [31].

Using the same longitudinal polished and etched specimens, a gold-pallidum sputter coating was applied and inclusion analysis by backscattered SEM images was performed by an independent lab, MEE (Materials Evaluation and Engineering, Inc., Plymouth, MN). The pixel resolution was 0.1255 μm yielding a particle resolution of 0.5 μm for a feature of at least 4 pixels wide. The lab analyzed 27 randomly selected images (96.38 μm × 128.51 μm) for each wire section. The Y-Feret data were used to estimate transverse inclusion size and density. The total area analyzed on the longitudinal sections was 0.334 mm^2 per wire by the independent lab.

Experimental Rotary Bend Fatigue and Imaging of Fractured Surfaces

Rotary bend fatigue tests of straight wire specimens were conducted on Blockwise Engineering Wire Fatigue Testers (Tempe, AZ) using a custom guided setup with one wire end being driven by a chuck and the other end remaining free as shown in Fig. 1. These experiments were performed on separate but identical setups by BSC and FDA. Specimens were bent around grooved mandrels made of polyoxymethylene (Delrin®) with varying radii through a 90° arc to generate fully reversed fatigue loading. The nominal alternating strains were calculated as

$$\varepsilon_a = \frac{d}{2(d/2 + \rho)}, \tag{3}$$

where ε_a is the nominal alternating strain, d is the wire diameter, and ρ is the radius of curvature of the mandrel. Imposed alternating strain varied from 2.63 to 0.27%. All tests were conducted at either 167 Hz (BSC) or 400 Hz (FDA) in phosphate buffered saline (PBS) maintained at 37 ± 2 °C to approximate in vivo conditions. Tests were run until fracture or until completion of 10^9 cycles which was considered runout.

After fatigue testing, a subset of fractured specimens was examined by SEM using a Hitachi S-3500N SEM or a Keyence VHX-7000 optical microscope at BSC and using a JEOL JSM-3690LV SEM at FDA. Prior to imaging, specimens were cleaned by sonication in a 70% ethanol solution for 15 min followed by an air-drying step. Images were taken of the entire fracture surface, with higher magnification images acquired at the fatigue crack initiation site. At FDA, image analysis, including dimensional analysis of non-metallic inclusions at the fatigue crack initiation site was conducted with ImageJ software [32]. At BSC, the inclusion dimensions were determined by measuring the major and minor axes of an ellipse that covered the inclusion.

Computational Modeling of Rotary Bend Fatigue Setup

Full three-dimensional finite element (FE) simulations of the rotary bend fatigue experiments were performed to (i) investigate potential variations in mechanics along the length of the wire specimens and (ii) estimate the cyclically transformed volume and surface area for each wire rotation (Fig. 1). All simulations were performed in ABAQUS R2016x for which rigorous code verification was recently performed [33]. Pseudoelastic behavior of the nitinol wire was modeled using the built-in superelasticity user material (UMAT) subroutine available in ABAQUS [34]. The constitutive model is based on the formulation of Auricchio and Taylor [35] and uses a mixture-type model to simulate the mechanical effects of stress-induced solid–solid crystallographic phase transformation between cubic (B2) austenite and monoclinic (B19') martensite. Material properties for the UMAT were extracted from ASTM F2516-18 [26] testing of two wire specimens performed at BSC. Specifically, a non-deterministic sequential random sample consensus (RANSAC) approach was implemented using Python/scikit-learn [36] and applied to perform multiple linear fits to the four approximately linear regions of the tensile data (austenite, upper plateau, martensite, and lower plateau). Average values for each material parameter were then computed and used as inputs to the FE simulations (Table 1).

Initially straight wires were discretized using a structured O–H mesh topology (Fig. 1) and hexahedral elements with incompatible modes (C3D8I) that are ideal for bending-dominated loading. Elements were generated with greater edge lengths in the long axis of the wire to reduce computational cost while limiting aspect ratios to approximately 4:1 to mitigate loss of element quality during the simulations. The wires were additionally coated in a one-nanometer thin skin of membrane elements (M3D4R) to facilitate the prediction of peak surface strains and the total surface area undergoing phase transformation during wire rotation. Mandrel and wire guide components were modeled as rigid analytical surfaces. Local material orientations were assigned in ABAQUS for all elements so that orientations of tensor-based quantities follow material deformations.

For each of the ten mandrels investigated, relative positions of the guides, the chuck, the mandrel, and the wire were assigned based on measurements from spatially calibrated digital photographs of the experimental setups. Frictionless contact constraints and displacement boundary conditions were used to move the initially straight wires into bent configurations (Fig. 1). Wire rotation was then driven using a tie constraint between the wire end and a virtual chuck surface with a prescribed angular velocity matching that used at FDA of

approximately 24,000 RPM (400 Hz). The implicit dynamic step formulation available in ABAQUS was used during simulation of wire rotation to mitigate snap-through instabilities that develop from a combination of wire torsion and contact interactions between the faceted wire surface and the virtual mandrel. A smoothed ramping step was also used to avoid undesirable dynamic effects generated by impulsively initiating wire rotation. Because the time scale for a single rotation of the wire is relatively small (0.0025 s), no time or mass scaling was needed to stabilize the simulations. To ensure convergence of hysteresis effects, three wire rotations were simulated, and quantities of interest were extracted from the final rotation. Field results were saved every $\frac{\pi}{50}$ radians for a total of 100 discrete results over the time interval $t \in \{t_{3s}, t_{3f}\}$, where t_{3s} and t_{3f} correspond to the start and end of the third rotation, respectively.

Quantities of interest were extracted from the simulation results using ABAQUS/Python scripting (Table 2). First, the portion of martensite fraction generated under mean hydrostatic tension was quantified as,

$$\hat{\zeta} = \begin{cases} \zeta & p > 0 \\ 0 & \text{otherwise} \end{cases}, \tag{4}$$

where ζ is the martensite fraction and p is the hydrostatic pressure defined as one-third the trace of the Cauchy stress tensor $\boldsymbol{\sigma}$, i.e., $p = \frac{1}{3}\mathrm{tr}\boldsymbol{\sigma}$. The total surface area and volume of martensite generated in tension during the final wire rotation were then calculated as,

$$A_{\mathrm{T}} = \sum_{i \in \mathrm{M3D4R}} \max_{t \in \{t_{3s}, t_{3f}\}} \left(\hat{\zeta}_i(t)\right) A_i, \tag{5}$$

$$V_{\mathrm{T}} = \sum_{i \in \mathrm{C3D8I}} \max_{t \in \{t_{3s}, t_{3f}\}} \left(\hat{\zeta}_i(t)\right) V_i, \tag{6}$$

respectively, where M3D4R and C3D8I are sets of Gaussian integration points for the respective element types, i is the integration point index, A_i and V_i are discrete areas and volumes $A_i = \frac{\mathrm{IVOL}_i}{d_{\mathrm{mem}}}$ and $V_i = \mathrm{IVOL}_i$, IVOL is the integration point volume available in ABAQUS, and d_{mem} is the membrane thickness.

Maximum strain amplitudes were next calculated for each integration point of the M3D4R element set, $i \in \mathrm{M3D4R}$. First, the maximum (ε_1) and minimum (ε_3) principal strains over all discrete time points of the final rotation were identified for each integration point,

$$\varepsilon_{1, \max, i} = \max_{t \in \{t_{3s}, t_{3f}\}} \left(\varepsilon_{1, i}(t)\right), \tag{7}$$

$$\varepsilon_{3, \min, i} = \min_{t \in \{t_{3s}, t_{3f}\}} \left(\varepsilon_{3, i}(t)\right). \tag{8}$$

Alternating and mean strain tensors [37] were then calculated using the full strain tensors associated with the maximum and minimum principal strains extracted above, i.e.,

$$\varepsilon_{alt,i} = \frac{\varepsilon_i(t_{\varepsilon 1,\max,i}) - \varepsilon_i(t_{\varepsilon 3,\min,i})}{2}, \tag{9}$$

$$\varepsilon_{mean,i} = \frac{\varepsilon_i(t_{\varepsilon 1,\max,i}) + \varepsilon_i(t_{\varepsilon 3,\min,i})}{2}. \tag{10}$$

Scalar alternating and mean strains were found by calculating the maximum eigenvalues $\varepsilon_{alt,i}$ and $\varepsilon_{mean,i}$ for all alternating and mean strain tensors $\boldsymbol{e}_{alt,i}$ and $\boldsymbol{e}_{mean,i}$. The polar coordinates of the integration points associated with these scalar strains were also extracted with the origin placed at the mandrel centroid. Finally, the globally maximum scalar alternating strain over all space was identified,

$$\varepsilon_{alt,\max} = \max_{i \in M3D4R} (\varepsilon_{alt,i}), \tag{11}$$

along with the corresponding scalar mean strain. Note that, because local material orientations were assigned in ABAQUS and were aligned with the long axis of the wire throughout the simulation, the directions of the principal alternating and mean strains are colinear and, thus, reorientation of the mean strain tensor as performed in the modified tensor method of Marrey et al. [37] for multiaxial loading was not required.

To estimate the numerical error in each quantity of interest, a quantitative mesh refinement study was performed for a smaller 12.9 mm radius mandrel given the associated larger strain gradients and greater mesh sensitivity with decreasing mandrel size. Three levels of mesh refinement were considered. From coarsest to finest, the number of elements spanning the wire diameter was 4, 8, and 16. Element counts in the long axis of the wire were similarly doubled for each refinement, yielding a consistent mesh refinement ratio of two. Simulations were then performed using each level of mesh refinement, and grid convergence indices (GCI) [38–40], representing 95th percentile confidence bounds on the numerical uncertainty, were calculated for each quantity of interest.

Results

DSC

The DSC specimen of the heat-treated wire had a mass of 30.0 mg. As shown in the bottom portion of Fig. 2, in cooling and heating, there were substantial R-phase transformations between the austenite and martensite phases. The $M \rightarrow R_{peak}$ was -1.4 °C and the $R \rightarrow A_{finish}$ (A_f) was 17.4 °C. The sum of enthalpies of the forward transformations, $A \rightarrow R$ 6.5 J/g and $R \rightarrow M$ 4.4 J/g, was approximately equal to the sum of the reversal transformations, $M \rightarrow R$ 7.5 J/g and $R \rightarrow A$ 3.2 J/g but substantially less than the $M \rightarrow A$ 23.0 or $A \rightarrow M$ 24.0 J/g transformations for ingot annealed 50.5 at.% Ni Nitinol [41]. Additionally, and related to the relatively low net enthalpy changes, the wide difference between the M_s and M_f temperatures is indicative of a high level of residual cold work in the material.

Surface Roughness Measurement

On the heat-treated and electropolished wire, the average surface roughness $\{R_a, R_z, R_{sm}\}$ measurements were $\{1.82 \pm 0.48, 10.1 \pm 3.4, 110 \pm 48\}$ μm circumferentially and $\{0.69 \pm 0.27, 6.1 \pm 2.6, 246 \pm 99\}$ μm longitudinally.

Hardness Testing

The Vickers hardness for the 25, 50, and 100 g loads ($N = 5$ each) was 358 ± 6, 347 ± 2, 336 ± 2 HV, respectively. The diamond shape of the indentation showed concave boundaries, i.e., "pin cushioning." The decrease in HV with increased load is attributed to a decreasing proportion of pseudoelastic recovery at higher forces, that is increasing plastic set with higher loads, since Vickers hardness is generally constant over this range in conventional metals (see Figure X5.6 in ASTM E384-17 [28]). Note that in "Inclusion-Based Fatigue Modeling in the Ultra-High Life Domain" section, we use the HV associated with the 100 g load. This is because we believe it is the most appropriate measure due to less pseudoelastic recovery and a longer and thus more accurate length measurement under the microscope.

Tensile Testing

Tensile testing of heat-treated wire revealed an austenite modulus of approximately 74.2 GPa, an average upper plateau stress of 465 MPa, and an average lower plateau stress of 231 MPa, with all values calculated based on engineering stresses and strains (see top portion of Fig. 2). The upper plateau began at a strain of approximately 0.70% and completed at about 6.7%. The ultimate stress was 1,322 MPa at uniform breaking strain of 10.8%. The initial (austenite) curve shape did not show any sign of an R-phase transformation. The reduction of area on fracture was $48 \pm 2\%$ ($N = 4$). Note that these values differ slightly from those used in the FEA simulations and shown in Table 1 since the parameters needed for FEA were extracted in Python by fitting linear regions to the same tensile data transformed to Cauchy stress and logarithmic strain.

Inclusion and Grain Size Analysis

From optical analysis and confirmed by SEM, the microstructure consists of very fine austenite grains with an acicular subgrain structure, with slight grain elongation and some banding of similarly oriented grain clusters in the longitudinal direction. Individual grains were not clearly defined at 1000× with the optical microscope and so a precise measurement of the average grain size could not be made. A visual estimate of the grain size is on the order of 2–5 μm.

The longitudinal measured percent inclusion areas were 0.84% by BSC and 0.75% by MEE (representative longitudinal and transverse images shown in Fig. 3). For inclusions greater than 2 μm^2, the percent areas were 0.65% and 0.54%, respectively. For inclusion lengths, the 99th percentiles were 18.2 and 12.18 μm and the maximums were 43.6 and 47.6 μm, respectively (see Fig. 4).

Transverse sections were also measured by BSC and the percent inclusion area for all inclusions identified to be 1.46%, 1.7 times the longitudinal percent area. The percent

transverse inclusion area for inclusions > 2 μm^2 was 0.64%, nearly identical to the longitudinal measurement.

For rotary bend fatigue, the stress concentration associated with inclusions (particle-void complex) is primarily a function of the transverse dimensions of the inclusion, not the longitudinal length. Therefore, we focus here on transverse inclusions though this ignores the importance of inclusion longitudinal length (e.g., stringer particle voids) which affect the probability of a fatigue crack initiating defect being located in a region at risk of fracture.

The maximum transverse inclusion length and Sqrt(area) from each image were tabulated and then used to estimate the largest inclusion in a given area at risk. The two parameters in the Gumbel extreme value distributions were as follows:

- For length, $\lambda = 5.73594$ μm, $\delta = 0.920991$ μm

- For Sqrt(area), $\lambda = 3.6684$ μm, $\delta = 0.53741$ μm

These distributions can then be applied to estimate the largest inclusion in the area at risk. This will be compared to the measured inclusions in the next section (see Fig. 5). In comparison with the location and scale parameters, the mean ± standard deviation of these metallographic image maximums is

Transverse length $d_{max} = 6.3 \pm 1.1$ μm;

Transverse Sqrt(area) $= 4.0 \pm 0.8$ μm.

Experimental Rotary Bend Fatigue and Imaging of Fractured Surfaces

Experimental fatigue test results are shown in the left side of Fig. 6. Note many UHCF (between 10^8 and 10^9 cycles) fractures and runouts to 10^9 cycles are observed.

Representative SEM images of fracture surfaces are shown in Fig. 7. We noted that the fatigue crack propagation area prior to ductile rupture as a percentage of the total fracture surface increased and then plateaued at about 50 to 60% as the imposed strain amplitude decreased; this is similar to the previous work [14]. Between specimens tested with the same size mandrel that fractured in low cycle fatigue (LCF) (~ 10^5 cycles) or UHCF ($> 10^8$ cycles), the fatigue crack percentage area was not substantially different and was in the 50 to 60% range.

All LCF and UHCF fractures visualized with SEM or optical microscope revealed inclusions at the fatigue crack initiation site. Figure 8 highlights the differences in observing transverse or longitudinal dimensions of inclusions. Taken from a specimen which was not included in the ε–N dataset due to a temperature controller problem, this specimen illustrates the importance of considering the inclusion transverse dimension as critical to fatigue crack initiation even though the longitudinal dimension may be larger. It should be noted that there appear to be circumferential scratches on the wire surface in Fig. 8. While such marks could be indicative of damage due to interactions with the mandrel, similar scratches were observed on untested wires (not shown) and so we do not believe that the Delrin mandrel itself was responsible for any of the observed fatigue fractures.

Except for one inclusion with a Sqrt(area) of 17.1 μm that was identified as an electropolishing defect and excluded from the ε–N dataset, the fracture site inclusions Sqrt(area) was approximately normally distributed from 1.9 to 12.6 μm, mean ± stdev of 7.4 ± 2.3 ($N = 57$). No clear trend differentiating the inclusion sizes in LCF versus UHCF fractures was observed with the exception of the highest alternating strain of approximately 2.6% that resulted in fatigue life between approximately 1000 and 2000 cycles; those three specimens tended to have smaller inclusions (3.3 ± 0.5 μm) at the initiation site compared to the other tested conditions. Beyond approximately 10^4 cycles, however, no clear relationship between inclusion size and fatigue life was observed. No difference was observed in inclusion size between FDA and BSC-tested specimens.

The length and Sqrt(area) of the inclusions can be compared to the estimated maximums from the extreme value analysis in the previous section. Graphically, Fig. 5 shows the largest Sqrt(area) inclusion on each of 27 metallographic sections are smaller than the crack initiating inclusions on the fatigue specimens. However, the individual areas analyzed in metallography, 0.043 mm^2, are much smaller than the areas at most risk of fracture in the rotating bend specimens and the maximum size inclusion would be expected to increase with area.

To determine the actual areas at risk, consider that in our fatigue apparatus each wire specimen is bent through a 90° arc around a mandrel. The upper bound for the area at risk is then the area of the wire in a 90° arc: $A_r = \pi\, d\, (r\, \pi/2)$ where d is the wire diameter and r is the mandrel radius. However, as seen in the FEA of "Computational Modeling of Rotary Bend Fatigue Setup" section, even in the elastic (no cyclic phase change) cases with nominal alternating strains ε_a of 0.62% or less, the nominal alternating strain value is achieved only over an arc of approximately 50° to 60°. For specimens with imposed ε_a less than 0.62%, we estimate the angle range with nominal strain increases from 53° to 60° and the area at risk increases from about 56 to 80 mm^2 as the strain amplitude decreases.

For specimens with cyclic phase change, ε_a greater than 0.62%, assuming cyclic phase transformation which locally generates higher strain amplitudes than the global nominal alternating strain to be the primary driver of fatigue, the area at risk decreases as the strain decreases from approximately 6 mm^2 to less than 1 mm^2 (see "Computational Modeling of Rotary Bend Fatigue Setup" section and Fig. 6). However, as discussed below in "Computational Modeling of Rotary Bend Fatigue Setup" section, the region of wire at strains near or above the nominal alternating strain increases as the cyclic phase fraction decreases. If the region of cyclic phase transformation shifts to the region with the largest inclusion in the region of near and above nominal strain, then, since the location of the largest inclusion is random, this increases the area at risk beyond the FEA-predicted area of cyclic phase transformation. We will assume the arc length approximately equal to the arc achieving the nominal strain. Thus, for specimens with cyclic phase change, the range of angle increases from 33° to 53° and the area at risk increases from about 8 to 55 mm^2 as the strain amplitude decreases.

With the areas at risk, A_r, modeled, we can use the extreme value statistics to predict the size of the largest inclusion. Herein, we conduct two types of comparisons between the

inclusion prediction and the fracture site inclusion measurement. First, we compare LCF and UHCF separately using their average areas at risk to compare the predicted LCF and UHCF average inclusions versus the average measured LCF and UHCF fracture surface inclusions. The goal of this exercise is to eventually use metallography data to predict the average size of inclusions which cause fracture. Second, from the sum of the areas at risk for LCF and UHCF specimens, we compare the predicted population largest inclusions versus the measured LCF and UHCF largest inclusions. The goal of this calculation would be to reliably predict, for a population of specimens, the maximum size of inclusion which causes fracture. Such statistics could be useful, for example, in helping assess the risk of fracture in populations of cardiovascular implant devices.

Of note, the inclusion size predictions are based on extrapolation from the distribution of largest inclusions measured in 27 metallographic areas. These metallographic areas A_o were each 0.043 mm^2. Compared to the individual wires' areas at risk, from 8 to 80 mm^2, the extreme value extrapolation's return period, $T = A_{\text{risk}}/A_o$, ranges from 180 to 1800. Summing all the fractography samples, the area at risk, A_{risk}, is approximately 30,000 times that of the metallographically examined area, A_0.

From the 37 LCF wires (cycles to failure less than 10^7) with inclusion data, the calculated areas at risk ranged from 8.0 to 67 mm^2 with mean $\pm$ population standard deviation (SD) = 37.8 ± 19.1 mm^2 ($N = 37$), and the predicted mean largest inclusion $\pm$ standard error of the estimate (SE) is 7.3 ± 0.5 μm. This compares well with the measured fracture site inclusion mean $\pm$ SD = 7.0 ± 2.2 μm ($N = 37$). Using the total population area at risk, $\Sigma A_r = 1400$ mm^2, the extreme value predicted largest inclusion at fracture sites mean $\pm$ SE is 9.2 ± 0.7 μm which underestimates the largest LCF measured fracture site inclusion of 12.0 μm.

From the 20 UHCF wires (cycles to failure greater than 10^7) with inclusion data, the calculated areas at risk ranged from 58 to 82 mm^2 with mean $\pm$ SD = 71.6 ± 8.2 mm^2 ($N = 20$). The predicted mean largest inclusion $\pm$ SE is 7.7 ± 0.8 μm. This compares well with the measured fracture site inclusion mean $\pm$ SD which is 8.1 ± 2.4 μm ($N = 20$). Using the total population area at risk, $\Sigma A_r = 1,431$ mm^2, the extreme value predicted largest inclusion at fracture site mean $\pm$ SE is 9.3 ± 0.9 μm, which, like the LCF prediction, underestimates the largest measured fracture site inclusion for the UHCF population of 12.6 μm.

Overall, the Gumbel extreme value model based on metallographic transverse inclusions predicted the average fracture initiating inclusion size within one standard error for both the LCF and the UHCF fractures when using the estimated average surface area of wire at or above the nominal strain suggesting that Eq. (2), $x(T = A_{\text{risk}}/A_o)$, is predictive. In contrast, the maximum of fracture site inclusion sizes was underestimated by the extreme value statistics. However, the calculations are for the expected values (means) of a population N $>> 1$ of approximately 1,400 mm^2 areas and thus not likely to be good predictors of $N = 1$ maximum values for all LCF or all UHCF fractures.

Computational Modeling of Rotary Bend Fatigue Setup

Mesh refinement studies performed for the 12.9 mm radius mandrel demonstrate all quantities of interest converge monotonically toward asymptotic values (Fig. 9). Based on

these results, the medium mesh discretization level with eight elements spanning the wire diameter was used in all simulations. For this discretization level, grid convergence indices (GCI) estimating the 95th percentile numerical uncertainty on simulation predictions are 11.4%, 4.7%, and 15.3% for maximum alternating strain, cyclically transformed area, and cyclically transformed volume, respectively.

Simulations predict the total cyclically transformed area and volume are zero for the largest three mandrels considered herein (right side of Fig. 6). For smaller mandrels, the cyclically transformed area and volume become finite and increase with decreasing mandrel radius, reaching maximum values of approximately 7.31 ± 0.35 mm^2 and 0.54 ± 0.08 mm^3, respectively (right side of Fig. 6).

The full three-dimensional wire rotary bend simulations also predict curvature and alternating strain values that vary along the length of the wires (Fig. 10). Specifically, in the wire segment wrapped around the mandrel, the wire radii of curvature are larger than nominal values toward the proximal and distal portions and slightly less than nominal toward the middle of the wrapped portion (Fig. 10). Conversely, predicted alternating strains are less than nominal values at the proximal and distal portions and higher in the middle of the wrapped segment (Fig. 10). Furthermore, differences between the nominal and predicted values increase with decreasing mandrel size, particularly for the predicted maximum alternating strains (Fig. 10 and Table 3). Also in Fig. 10, the angular locations of experimental fatigue fractures are overlaid at the top of each maximum alternating strain result; good alignment is observed between predicted locations of relatively higher strain and experimental fatigue fracture locations.

Discussion

This Discussion is organized into three main sections. Given the large amount of fatigue data including both fractures and runouts, "Reliability Modeling of ε–N Data" section is dedicated to describing the statistical analysis of our data including both one- and two-failure-mode models for representing the bimodal behavior of LCF and UHCF fractures. "Inclusion-Based Fatigue Modeling in the Ultra-High Life Domain" section further analyzes the UHCF fractures and utilizes a damage growth model from high-strength steel combined with geometrical and material information from our nitinol specimens to predict a safe loading level that agrees well with the observed fatigue life. Lastly, "Discussion of Computational and Experimental Fatigue Results" section compares our fatigue results to other publications including an examination of potential mechanistic differences between LCF and UHCF in nitinol.

Reliability Modeling of ε–N Data

It is a standard practice to fit fatigue data using probability distributions in order to estimate the expected reliability of the samples throughout the range of loading. For a review of some of the methods, see Castillo and Fernandez-Canteli (2009) or Meeker et al. (in preparation) [42, 43]. In this section, two alternative fatigue models were fit to the fatigue data in Fig. 6. The first model imposes a single failure mode while the second assumes that there are dual

competing failure modes. The purpose of this exercise is to debate the value of interpreting the data either as a single failure mode or as two separate failure modes.

The Non-Competing Single Distribution Model—Coffin-Manson Strength Model—There are two basic ways to describe the statistical variability in fatigue performance: life distribution and strength distribution. On a typical ε–N diagram, the life distribution appears horizontally, and the strength distribution appears vertically. Both life and strength distributions have important roles in a practical understanding of fatigue. The life distribution is the probability that a fracture will occur at a number of cycles under an applied strain level. The strength distribution is the probability that a strain level will cause fracture at a given life.

Historically, the probability distribution is constructed by proposing the mathematical form of the life distribution, e.g., lognormal or Weibull. This implies that the test samples all fail due to this single distribution. It is well known that life-based models which attempt to capture the variability in life with one life variance parameter perform poorly when applied to data of the type that has larger changes in ε–N slope, as seen in our 10^9 cycle nitinol dataset. Alternatively, single distribution fatigue models may be constructed with one strength variance parameter as given in Falk 2019 [44]. This method has benefits in terms of goodness of fit to fatigue data showing substantial changes in ε–N function slope, as is observed with nitinol and stainless steel. In addition, the method allows the statistical implementation of the Coffin-Manson function as well as other well-known functions. Variation in strength was modeled as lognormal. The standard deviation of the strength distribution, s, is the single parameter which attempts to bracket the data scatter in the observed lifetimes of samples tested at all strain levels. The standard Coffin-Manson model relates median strength $\bar{\varepsilon}$ as a function of life, N,

$$\bar{\varepsilon}(N) = A_{el}(2N)^b + A_{pl}(2N)^c \tag{12}$$

where parameters b and c are, respectively, the limiting slopes of the high cycle and low cycle segments on a log–log plot. The significance of parameters A_{el} and A_{pl} is the intercept of the high cycle and low cycle segments on a log–log plot.

Surrounding the Coffin–Manson function at any value of life, N, there is a lognormal strength distribution with the log mean of the distribution given by $\bar{\varepsilon}(N)$. The lognormal strength distribution is assumed to have constant variability in strength, s, regardless of the value of life. In this construction the failure CDF $F(N/\varepsilon)$, the probability that a sample tested at strain ε will fail prior to cycle N, can be written using the standard normal CDF $\Phi(x)$[1]

$$F(N \mid \varepsilon) = \Phi\left(\frac{\log\varepsilon - \log\bar{\varepsilon}(N)}{s}\right) \tag{13}$$

---

[1]$\Phi(x) = P(Z \le x) = \frac{1}{\sqrt{2\pi}} \int_{-\infty}^{x} \exp\left\{-\frac{u^2}{2}\right\} du.$

To summarize this model, the five statistical model parameters used are as follows: $\{A_{el}, b, A_{pl}, c, s\}$. The first four define the Coffin-Manson ε–N curve and the last defines the standard deviation of the strength distribution. The maximum likelihood estimate (MLE) is the choice of model parameters that maximize the likelihood of the observed lifetime versus strain data. These parameters were fit to the fatigue data using standard maximum likelihood estimation techniques implemented in MATLAB. This technique allows for the analysis of fracture and censored data. The confidence intervals were determined for each parameter using the profile likelihood methodology, defining the confidence interval for each scalar parameter as the highest and lowest value which maintains negative log-likelihood within limits based on the chi-squared distribution. For the 95% confidence interval, the limit corresponds to 1.92 log-likelihood units.

The results of this analysis are shown on the top of Fig. 11. From a statistical perspective, the overall fit is good. However, unlike the sparse fracture data in the 10^5 to 10^8 cycle range, the single-mode curve predicts a continuous distribution of fracture counts for strains from about 0.5% to 0.6%. To model the bimodal data, that is the sparsity of fracture counts between 10^8 and 10^5, an "8 to 5 gap," a two-failure-mode model is considered.

The Competing or Two-Failure-Mode Model—The ε–N data for some materials indicate the presence of competing failure modes [45]. This characteristic fatigue behavior exhibits the typical trend of increasing life with decreasing strain amplitude. However, the trend reaches a threshold strain below which fatigue life extends dramatically. Near this threshold, a bimodal life distribution emerges. At still lower strain amplitudes, fatigue life becomes very long. If the test is carried out for a sufficient duration below this threshold, fatigue fractures still will occur. The ε–N curve will again show a dependence of increasing life with decreasing strain amplitude in the long-life region. Often the test duration is not carried out beyond 10^7 cycles experimentally; therefore, this second slope will not be detected leading some to mistakenly assert an infinite fatigue life stress or strain threshold.

For some materials, these two-failure modes present different fractography. This behavior is seen in a variety of high-strength materials including steels, titanium alloys, and nickel-base superalloys [46]. Although no obvious fractographic differentiation has been detected for nitinol in our study, the threshold strain coincides with the onset strain of martensitic transformation. Therefore, we assume that the high amplitude failure mode is due to repeated cyclic martensitic transformation while the lower amplitude mode is not.

An appropriate way to model this behavior is a competition between failure modes, resulting in two separate ε–N curves, one for higher amplitude mode and the other for longer life mode. Models of this type have been used previously for various applications, for example, in electronics [47]. Here, we will derive a simplified version of the competing failure model applied to fatigue, which was presented by Paolino et al. [48].

For the sake of simplicity, the median cycles to fracture for each mode is modeled to have an inverse power law dependence on strain.

$$\text{Mode1:} \quad \overline{N}_1(\varepsilon) = w_1(\varepsilon)^{m_1} \tag{14}$$

$$\text{Mode2}: \overline{N}_2(\varepsilon) = w_2(\varepsilon)^{m_2} \qquad (15)$$

In other words, for each fracture mode, the dependence of life on strain amplitude is linear on a log–log plot with slope, w_i, and intercept m_i. Surrounding each of these function at any value of life, N, there is a lognormal life distribution with median $\overline{N}_i(\varepsilon)$ for $i = 1;2$. The lognormal distribution is assumed to have constant variability in life, s_i. Therefore, the failure CDF for each mode can be written using the standard normal CDF $\Phi(x)$

$$\text{Mode1} : F_1(N \mid \varepsilon) = \Phi\left(\frac{\log N - \log \overline{N}_1(\varepsilon)}{s_1} \right) \qquad (16)$$

$$\text{Mode2}: F_2(N \mid \varepsilon) = \Phi\left(\frac{\log N - \log \overline{N}_2(\varepsilon)}{s_2} \right) \qquad (17)$$

To complete the model, we need to implement the threshold strain above which Mode 1 is active and below which it is not. To accomplish this, a logistic step function $\rho(\varepsilon)$ governs the fraction at risk of fracture due to Mode 1, for a given strain level

$$\rho(\varepsilon) = \left[1 + \exp\left(\frac{\log \varepsilon_{50} - \log \varepsilon}{q} \right) \right]^{-1} \qquad (18)$$

The two parameters controlling the transition are ε_{50}, which is the strain level midway through the transition where 50% of the samples are at risk, and q, which determines the span of the transition. Now putting all the two-mode model pieces together, the probability a sample will fracture by either mode for a given strain and cycle count is one minus the probability that the sample will survive both modes

$$F_{1\&2}(N \mid \varepsilon) = 1 - (1 - \rho(\varepsilon) \times F_1(N \mid \varepsilon)) \times (1 - F_2(N \mid \varepsilon)) \qquad (19)$$

To summarize the two-failure mode model, the eight statistical model parameters used are as follows: $\{ w_1, m_1, s_1, w_2, m_2, s_2, \varepsilon_{50}, q \}$. As before, maximum likelihood techniques were used to determine the parameters and confidence bounds.[2] Results of this analysis are shown on the bottom of Fig. 11. In Fig. 12, the empirical cumulative distribution functions (eCDF) for the experimental data at six alternating strain levels are compared with the two-mode model fit. The eCDFs are generated by sorting the n data points at each strain level from the smallest to the largest cycles to fracture, N_m from $m = 1$ to n, and then plotting $\{\text{Log10}(N_m), (m - 0.5)/n\}$ for $m = 1$ to n. The graph illustrates that the two-mode model captures the

---

[2]Due to numerical convergence issues, the parameter ε_{50} was "hard" set to 0.56% strain rather than identified using maximum likelihood techniques. This choice for ε_{50} was based on inspection of the observed cycles to fracture data. Samples run at this nominal strain level of 0.56% saw roughly equal proportions fracture before and after 10 million cycles. As a result of setting the parameter, the fit of the ε_{50} parameter may not be optimal, and the confidence bounds on ε_{50} could not be calculated. Work to improve the numerical algorithm to treat ε_{50} as a true model parameter is ongoing.

paucity of data between 10^5 and 10^8 cycles. The one-mode model does not capture the "8 to 5 gap."

Inclusion-Based Fatigue Modeling in the Ultra-High Life Domain

The fatigue fractures we observed in UHCF ($N^> 10^7$ cycles) provide valuable data which can be analyzed by fatigue models that are used for UHCF fractures in steels [22, 23, 49–51]. Key to this methodology is determining the crack propagation threshold K_{th} and a damage curve that estimates an adjusted increase in inclusion length as N increases beyond 10^7 cycles. Thus, in this section, we use our UHCF $R = -1$ fracture surface inclusion's area as well as the associated alternating strain and cycles to failure to estimate (i) the classical linear elastic fracture mechanics crack propagation threshold for $R = -1$ and (ii) the growth of cracks from inclusions in the subclassical microstructural crack domain that lead to fracture in the UHCF domain.

For a simple model, we assume for fatigue lives longer than 10^7 cycles that the stresses and strains are less than the plateaus and the stress and strain relationship is elastic, linear, and symmetric in tension and compression for our loading ratio of $R = -1$. Using this assumption, we can convert the strain amplitudes to stress amplitudes by using the measured elastic modulus $E = 74,200$ MPa:

$$\Delta\sigma_a = E \cdot \Delta\varepsilon_a \tag{20}$$

For predicting the crack propagation threshold K_{th}, from inclusions, the Murakami-Endo Model predicts that when the location of the fracture origin is a small defect such as a non-metallic inclusion then the fatigue limit for $N^< 10^7$ of the material can be determined by the Vickers hardness of the microstructure surrounding the non-metallic inclusion and the square root of the projected area (area) of the defect normal to the stress [49]. For $R = -1$, measured 336 HV (100 g, 10 s hold) and measured UHCF mean fracture face inclusion 8.1 μm ($N = 20$), the Murakami predicted $K_{th,M}$ is given by

$$\Delta K_{th,M} = 3.3 \times 10^{-3} \times (HV + 120)(\sqrt{area})^{1/3}$$
$$= 3.02 \text{MPam}^{1/2} \tag{21}$$

and the corresponding $^< 10^7$ fatigue life stress,

$$\sigma_{wl} = \Delta K_{th,M}/(\sqrt{area})^{1/2}, \tag{22}$$

$$\sigma_{wl} = C \cdot (HV + 120)/(\sqrt{area})^{1/6} = 460 \text{MPa}, \tag{23}$$

where we used $C = 1.43$ for inclusions on the surface of a test specimen. Other values recommended are $C = 1.41$ for inclusions in contact with the surface or 1.56 for inclusions underneath the surface. In Eqs. (21)–(23), the units for HV are kg/mm^2 and for sqrt(area) are μm. The corresponding alternating strain is

$$\varepsilon_{wl} = \frac{\sigma_{wl}}{E} = 0.00620. \tag{24}$$

As a comparison to the Murakami–Endo Model for stress intensity, if we limit our analysis to the UHCF domain to apply linear elastic assumptions, we can calculate the range of stress intensity factors from the sizes (area) of the inclusions at the fatigue crack initiation sites and the associated strain amplitudes. For the 20 fractures at greater than 10^7 cycle, we calculate [49]

$$\Delta K = Y \cdot E \cdot \Delta \varepsilon_a \cdot \sqrt{\pi \cdot \sqrt{\text{area}_{\text{inclusion}}}}, \tag{25}$$

where K is the stress intensity factor and Y is a geometrical factor equal to 0.65. For these fracture site inclusions based on area, which for UHCF ranged predominately from 5.4 to 12.6 μm, the corresponding K ranged from 1.09 to 1.56 MPa m$^{1/2}$ (predominately because we called the singular 1.9 μm inclusion an outlier). As per Eq. 25, K is a linear function of the strain amplitude (0.48% to 0.60%) and area$_{\text{inclusion}}^{1/4}$. We detected no relation between the log10 number of cycles to failure and K, $R^2 = 0.032$ for a linear fit.

These UHCF Ks are less than the K_{th} predicted by the Murakami-Endo model for LCF. However, over 10^7 to 10^9 cycles, it may be reasonable to assume that sub-threshold crack growth occurs from inclusions until, perhaps, K_{th} is exceeded resulting in crack propagation and fracture. If true, then to predict fatigue from inclusions, we need a model for sub-crack propagation threshold crack growth.

To develop this model for UHCF fracture from inclusions in high-strength steel, Murakami and associates investigated heat-treated hard steel (Cr–Mo steel SCM435) in $R = -1$ tension–compression in the domain of $N = 10^5$ to 5×10^8 cycles. With heat treatment and quenching, the samples were case hardened, with surface compressive residual stress leading to fatigue cracks growing from the softer core. Examination after fracture showed the fracture face initiation inclusion was surrounded by a different texture surface, identified as the Optical Dark Area (ODA), beyond which the texture was of typical cyclic fatigue facture morphology. Using the ODA as the threshold crack initiation defect, the increase of the defect size relative to the initial inclusion defect size can be used as a measure of damage:

$$\begin{aligned} Damage &\equiv (\text{original defect size} + \text{growth})/(\text{original defect size}) \\ &= (\text{ODA})^{1/2}/(\text{inclusion area})^{1/2} . \end{aligned} \tag{26}$$

Measuring *Damage* as a function of the number of fatigue cycles, it was fit by the following curve [52]:

$$Damage(N) = 1.236 - 0.4542 \cdot \log_{10}(N) + 0.08237 \cdot \log_{10}(N)^2 . \tag{27}$$

Roughly, the damage ratio equation in the range from $N = 10^7$ to 10^9 increases linearly with $\text{Log}_{10}(N)$ from 2.1 to 3.8. The prediction of the fatigue strain amplitude, $\varepsilon_{a;p}$, beyond 10^7 using the Murakami–Endo model (Eq. 23) and the damage model (Eq. 27) is given by

$$\varepsilon_{a,p} = \sigma_{wl}(\sqrt{\text{area}} \cdot Damage(N))/E$$
$$= C \cdot (HV + 120)/(\sqrt{\text{area}} \cdot Damage(N))^{1/6}/E, \tag{28}$$

where the inclusion size $\sqrt{\text{area}}$ in Eq. 23 is increased over N cycles by the damage growth model. Naively applying this model to our nitinol rotary bend results, using the average inclusion size $\pm$ 2 standard deviations (excluding the 1.9 μm outlier), we generate the curves in Fig. 13 to compare to the UHCF rotary fatigue test results. Observing the life based on the mean inclusion size of 7.4 μm, the predicted fatigue strain amplitude decreases from 0.6% at 10^6 cycles to 0.5% at 10^9 cycles, comparing well to the UHCF data.

The experimental fracture site inclusions based on area ranged overall from 1.9 to 12.6 μm ($N = 57$), and predominately from 5.4 to 12.6 μm ($N = 19$, 1.9 μm outlier excluded) in the UHCF domain. This compares with Urbano's measured $\sqrt{\text{area}}$ rotary bend induced fracture site inclusions for five different types of superelastic nitinol wire sets that approximately ranged from the most fatigue resistant at 10^6 cycles with Sqrt(area)s of approximately 2.0 to 5.5 μm to the least fatigue resistant at 10^6 with Sqrt(area)s of 2.4 to 10.7 μm [17]. As in our testing, they saw inclusions at the origin of all fractures. However, Urbano et al. observed, unlike us, that at a given test strain level, the fracture site inclusions were larger for earlier breaks than for later breaks; e.g., at 0.9% strain, the first break at around 10,000 had a 3.8 μm inclusion whereas the last break at around 30,000 had a 2.0 μm inclusion.

The Murakami crack propagation threshold based on HV and the mean fracture face inclusion area is 3.02 MPa m$^{1/2}$. This is about 1.5 times McKelvey and Ritchie's K_{th} = approximately 2.1 MPa m$^{1/2}$ for superelastic austenite nitinol disk-shaped compact tension ASTM E674–12 [53] specimens at a load ratio $R = 0.1$ [54]. Urbano estimates K_{th} at $R = -1$ is approximately 4.0 MPa m$^{1/2}$ with a lower bound of 2.2 MPa m$^{1/2}$ by using Schijve's equation to extrapolate from Robertson and Ritchie's measurements on medical tubing NiTi fabricated CT samples for $R = \{0.7, 0.5, 0.1\}$ [17, 55, 56].

While these are comparable, they do not appear to compare well to our measured UHCF K's where K ranged predominately from 1.09 to 1.62 MPa m$^{1/2}$. However, applying the damage model to account for the increased UHCF growth in area sub-threshold K,

$$\Delta K_{adj}(N, \Delta\varepsilon_a, \text{ area}_{\text{inclusion}})$$
$$= Y \cdot E \cdot \Delta\varepsilon_a \cdot \sqrt{\pi \cdot Damage(N) \cdot \sqrt{\text{area}_{\text{inclusion}}}} \tag{29}$$

the average damage adjusted measured $K_{adj} = 2.30 \pm 0.23$ MPa m$^{1/2}$ and ranging predominately from 1.95 to 2.74 MPa m$^{1/2}$ ($N = 19$, excluding the outlier at an adjusted 1.06 MPa m$^{1/2}$). This predicted damage K_{adj} for the UHCF specimens is below Murakami model's $K_{th,M}$ prediction but close to Urbano's lower bound K_{th} estimate of 2.2 MPa m$^{1/2}$ for $R = -1$.

The next calculated Murakami model prediction was for the $< 10^7$ fatigue limit stress. The prediction of 460 MPa compares well to the measured average upper plateau stress of 465 MPa and the knee of the ε–N curve. This is interesting but likely a coincidence for they are very different phenomena. One is a temperature-dependent phase transformation stress and the other is a fatigue life stress prediction based on HV for a material without cyclic phase change (high-strength steel). If, however, the predicted $< 10^7$ fatigue limit stress was below the plateau, then fatigue failures may occur in the low cycle domain without cyclic phase change. In UHCF, the Murakami model prediction for the $< 10^7$ fatigue limit stress provides an upper bound to the UHCF strain amplitude σ_{wl} by the modulus yields a strain amplitude of 0.641% which is above the maximum strain amplitude for any fracture greater than 10^7—the largest observed strain amplitude for fractures above 10^7 was 0.596% at $10^{7.9}$ cycles.

Perhaps most interestingly, the naive application of the high-strength steel damage model into the Murakami-Endo fatigue life model, Eq. 28, with the mean $\pm$ 2 standard deviations of measured fracture site inclusion area from all the fractures ($N = 57$) did a reasonable job in predicting the slope and range of UHCF fractures especially considering no coefficients in the equations were changed from the Murakami et al. work with high-strength steel.

While the accuracy of the predictions is remarkable and likely at least partly a coincidence, there are common mechanisms. First, the use of Vickers Hardness provides a measure of the resistance of the metals to plastic deformation. Second, the area is a simple way to account for the stress concentration associated with the inclusion. Third, we speculate that the UHCF growth of the crack might be due to a common embrittling element—hydrogen—that appears due to corrosion/oxidation at the crack front.

Murakami provides evidence that UHCF growth in high-strength steel is based on the diffusion of hydrogen from inclusions to the crack tips initiating from those inclusions [50, 51]. For nitinol, Racek et al. investigated hydrogen transport and mechanisms by which hydrogen affects the crack nucleation and growth in nitinol wires [57]. They observed that major cracks always nucleated at inclusions or notches on the surface of the wires where corrosion may initiate. From potentiodynamic experiments, Sun et al. found that corrosion breakdown occurs in fractured Ti_2NiO_x inclusion particle-void "pits" and adjacent to TiC inclusions (which are cathodic to the NiTi matrix) [58]. More locally to the crack front, in tests in aqueous solutions, hydrogen ions are created by the oxidation of newly exposed crack faces, $Ti + 2H_2O \rightarrow TiO_2 + 4 H^-$, and it is plausible that sufficient numbers of those free hydrogen ions are absorbed into the matrix embrittling the crack region. Then episodically the embrittled crack grows which over time leads to a crack length with stress that exceeds K_{th} for the matrix leading to fracture. Electropolishing of nitinol might also increase hydrogen in the matrix which over 10^7 to 10^9 cycles may preferentially diffuse to the high strain crack front in a time scale similar to hydrogen creating damage in steels. Though the materials and loads are different than in Murakami's high-strength steel tension–compression experiments done in air, we speculate it might be a common mechanism – hydrogen embrittlement that leads to crack growth and fracture [50, 51].

While we speculate that hydrogen from corrosion may play a role in crack initiation and sub-threshold crack growth, its role may be as a secondary embrittling agent to the fundamental role that microstructure and prior processing play. We suspect that cold work drawing processes may generate cracks at matrix-inclusion interfaces. Then, when a nitinol material like ours is tested at high cyclic strains, in the LCF domain, we suspect the crack propagation threshold is exceeded for the cracks at large inclusions from the beginning of the test. Alternatively, if not exceeded at the start of loading, cyclic phase change-induced damage rapidly grows the crack over the threshold leading to an LCF fracture. In the UHCF domain, we interpret our results as suggesting it may take 100 s of millions of cycles of sub-threshold crack growth to reach threshold. However, this discussion is speculative since the actual mechanism(s) were beyond the scope of this study.

A damage model as a function only of inclusions size and number of cycles in UHCF based on the growth of preexisting inclusion cracks to the point where the nitinol matrix's K_{th} threshold is exceeded would be a convenient way to predict fatigue life. It is remarkable, and we suspect at least partially a coincidence, that this model worked for our material at small dimensions with inclusions at the surface, most unlike the high-strength steel tension–compression specimens on which the damage model was first determined. The microstructural mechanisms, prior processing, corrosion, and the rates by which sub-threshold small cracks grow in nitinol resulting in UHCF fractures need to be studied further to develop robust predictions as well as guide the development of more robust nitinol devices. Lastly, it is worth noting that although we may wish to use Eq. 28 to predict the limiting value of alternating strain for say 600 million cycles life with, for example, a 10 μm inclusion, such an equation is not physical. Physically, the fatigue life N is a function of the alternating stress–strain, cyclic phase transformation if present, the inclusion size in the volume at risk, and some mechanism(s) for advancing the crack through the local grain structure until the macroscopic K_{th} threshold is exceeded. Reversing the independent and dependent variables is erroneous thinking and may result in poor statistical modeling [43].

Discussion of Computational and Experimental Fatigue Results

Here, we discuss our fatigue results in light of what we learned in analyzing our data and by comparison to literature. First, we look at the calculation of strain from FEA and see that it provides insight on the stress–strain spatial distribution and the effects of the phase transformation that an estimate from the textbook bending equation does not. Next, as others have seen by comparing tensile upper plateau strains, we show that the presence of a cyclic phase transformation appears to limit the fatigue life to about 10^5 cycles. We then note that though many experimentalists test to 10^7 cycle runout, extrapolating that the runout is an indicator of an infinite fatigue life is incorrect. Additionally, for test prediction and planning beyond 10^7 cycles, a two-failure-mode fatigue model which has the bimodal LCF and UHCF cycles to fracture may be preferential to the classic Coffin-Manson model or other single-mode models.

In our calculations for alternating strain, we relied on Eq. 3 in "Experimental Rotary Bend Fatigue and Imaging of Fractured Surfaces" section which estimates the alternating strain in terms of the wire diameter and radius of curvature as measured from the mandrel center

to the bent wire's centerline. This equation assumes i) a constant radius of curvature and ii) symmetric linear elastic stress–strain relation. Accordingly, the equation produces similar values to the commonly used

$$\varepsilon_{\mathrm{a}} = \frac{d}{2\rho} \qquad (30)$$

as described in ASTM E2948–16A [59] and used in other publications on rotary bend fatigue [9, 20]. Neither of these equations, however, considers the unique non-linear mechanical response of nitinol and therefore likely under-predicts alternating strain for the smaller mandrels where cyclic phase transformation is occurring.

For a direct comparison, Table 3 highlights the estimated alternating strain values using either Eq. 3 or the FEA for some of the mandrels used in our experiments. At low alternating strain values below approximately 0.62% (i.e., the value where austenite begins to convert to martensite in our FEA simulations), the different methods result in very similar alternating strain values. For larger alternating strain values, i.e., for wires on smaller mandrel radii, the alternating strain estimations diverge from one another as the peak martensite fraction increases. When analyzing these data, it is important to note the unique nature of our FEA which incorporated measurements of the relative positions of the wire to the mandrel and guides from spatially calibrated digital photographs of the experimental setups. This is important because if the relative locations of these components are adjusted, the wire position will conform differently around the mandrel radius which affects the resulting wire curvature (Fig. 10) over theta and thus the alternating strain as calculated by the FEA. This is most noticeable for Mandrel VIII in Table 3, which is the only mandrel with an alternating strain below the elastic limit where the FEA and the analytical equation diverge. This is likely due to how that particular mandrel fit in with the horizontal and vertical guides; because of its size, there was an additional unsupported length on either end of the curved mandrel which had some minor effects on the imposed bend.

Also of note in Table 3 from the FEA calculations is that at smaller mandrel radii, the assumption of zero mean strain begins to break down and a small positive mean strain is observed. Mean strain increased monotonically from largest to smallest mandrel with the exception of Mandrel **VIII** which, as mentioned above, had slightly different unsupported lengths than the other mandrels. It is worth nothing, however, that the mean strain calculated by FEA for Mandrel **VIII** was still very close numerically to the next smallest and next largest mandrel, suggesting that any differences in the unsupported wire length had minimal effect on mean strain. While the absolute value of the mean strain is relatively small compared to the corresponding alternating strain value, it is important to note as it may improve understanding of how mean strain affects the fatigue life of nitinol [3, 60]. Lastly, we note that the values from our FEA simulations have not been validated against an experimental comparator like digital image correlation [61]. Thus, while we expect the observed relative trends from our simulations to be correct, the absolute values have not been validated. Indeed, the present study motivates the investigation of direct strain measurements in situ with rotary bend wire fatigue experimental setups in future work,

especially for testing involving smaller mandrels for which the FEA herein predicts larger deviations from analytical strain estimations calculated using Eq. 3.

In Fig. 6, a clear transition (i.e., knee) from LCF to UHCF can be observed at approximately 0.62% alternating strain. At strains above this value, experiments resulted in fatigue life of roughly 10^5 cycles or fewer. Between 10^5 and 10^8 cycles, relatively few fractures are observed. While all fatigue cracks in both LCF and UHCF observed (Figs. 7 and 8) appeared to initiate from inclusions, we suspect that different mechanisms are occurring. Around the 0.62% alternating strain value, there is a transition where some LCF fractures are observed and some UHCF fractures are observed around 10^8 cycles. It may be the case that for certain specimens, the particular grain size and orientation, inclusion geometry, the inclusion-matrix interface, and other microscale features are favorable to creating cyclic phase transformation resulting in LCF whereas other specimens may happen to not have those characteristics and, thus, UHCF is observed.

At an alternating strain of approximately 0.48%, fractures are observed solely in the UHCF region above 10^8 cycles as well as some runouts to 10^9 cycles. Above approximately 0.62% alternating strain, cyclic phase transformation increases (demonstrated by transformed volume and area seen in Fig. 6) and the observed fatigue life decreases. As shown in Fig. 6, this experimental knee corresponds approximately to the strain value where cyclic phase transformation begins. Mechanistically, we suspect that different phenomena are leading to fatigue fractures in the LCF domain as compared to the UHCF domain wherein LCF fractures include rapid damage development due to cyclic phase transformation and UHCF fractures accumulate damage resulting in sub-threshold crack growth over hundreds of millions of cycles. Future work should attempt to elucidate the actual mechanism of this damage accumulation to better understand the important factors leading to UHCF fractures. Also notable in our experimental results, as seen in Fig. 6, is the agreement between the two laboratories with a high amount of overlap in fatigue life suggesting high reliability in the data even with different equipment and operators.

Several prior investigations have characterized the fatigue behavior of nitinol with respect to the phases present at the respective test temperatures and the imposed alternating strains [8, 9, 11, 62]. In the low cycle domain, less than 10,000 cycles, clear regions of strain amplitudes on the ε–N curve correspond to strains above the upper plateau, on the plateau, and below the plateau. Rahim et al. 2013 observed a transition from LCF to UHCF of nitinol in rotary bend fatigue around 1.2% assuming the wire was bent into a circular arc between the two supports [20]. This 1.2% strain was approximately equal to the value at the beginning of the upper stress plateau for their high-purity nitinol material. Catoor et al. 2019 studied tension–tension fatigue of nitinol specimens under two types of loading – the first case being a nominally elastic deformation without cyclic hysteresis and the second case with large enough deformation to cause cyclic stress-induced martensite transformation. When categorizing the two loading scenarios this way, loading with cyclic stress-induced martensitic transformation was observed to cause fatigue fractures in roughly 10^5 cycles or fewer whereas loading of the nominally elastic case resulted in mostly runouts to 10^7 cycles. Thus, even though the loading mode was different than in our experiments, the results of Catoor et al. align with ours with cyclic phase transformation leading to fractures occurring

at or before about 10^5 cycles and without cyclic phase transformation fractures do not occur until at least 10^7 cycles. Put another way, mandrels with radius small enough to cause cyclic phase transformation as observed in our FEA simulations (Fig. 10) corresponded to fatigue life of 10^5 cycles or fewer. Further literature and experimental investigation on the relation of the strain at the beginning of the martensite phase transformation, $A \rightarrow M$ or $R \rightarrow M$, in tension test and the transition from LCF to UHCF may be useful for design heuristics.

While we have attempted to present an exhaustive body of work and thorough analyses, it is important to note some limitations. Although rotary bend fatigue has allowed for the relatively quick evaluation of fatigue life out to one billion cycles, the loading mode does not permit the evaluation of different mean strains that are relevant and important for nitinol fatigue characterization, especially for implantable medical devices. Future work should focus on different specimen types capable of evaluating mean strain as an independent variable.

In reviewing our material characterization results, we have begun planning future work which will include some changes to obtain more relevant and useful data. For the Vickers hardness tests, which could facilitate assessing medical devices material directly, we plan to use higher loads to reduce the influence of superelastic recovery on the final indent size, thus producing a more accurate estimate of nitinol's resistance to plastic deformation. We plan to measure in the direction of the bending stresses which is on the transverse surface. Additionally, we plan on assessing the HV close to the outer diameter surface versus the center in case there is variation in hardness with depth. For grain size assessment, we plan to use electron backscattering diffraction (EBSD) in the future since optical techniques did not provide discernable grain sizes. For metallographic inclusion measurements, we plan to develop a method to assess separately the largest transverse Ti_2NiO_x and transverse TiC inclusions as the distributions may be different and their impact on fatigue life may differ. In the determination of size, we would consider metrics other than Sqrt(area) to better account for the shape on the stress generated and the crack growth rate. We hope that these changes might help us better understand why we did not see shorter inclusions surviving longer than longer inclusions at a given strain level. Additionally, we plan to use energy-dispersive X-ray spectroscopy (EDS) to distinguish between oxide and carbide inclusions on fractured surfaces that led to fatigue crack formation.

Finally, though we found good agreement between the Gumbel Extreme value prediction of the mean LCF and UHCF inclusion sizes, we did not predict accurately the maximum or, more generally, the upper tail of the fracture site inclusions. We will be investigating the model and our assumptions to improve agreement. For risk assessment, the largest inclusion may not be what matters for crack initiation. Instead, for UHCF what matters includes both alternating stress or strain and the area density of inclusions of sufficient size and probability of initiating sub-critical cracks that grow.

This work was limited to the evaluation of one set of nitinol specimens and it is unclear exactly how different processing and/or surface finishes might affect UHCF. Future work from our group will include similar experiments on higher purity and differently processed nitinol to gain further insights into fracture mechanisms in the LCF and UHCF domains.

We hope this will facilitate predictive comparisons of LCF and UHCF domains between different nitinol materials and thus provide important information on the predictive utility of the Fatigue to Fracture methodology as described in ASTM F3211–17 [63].

Conclusions

In this first of a kind study to examine medical grade nitinol fatigue out to one billion cycles, we have employed a wide range of experimental, analytical, and computational techniques. The principal conclusions of our study are as follows:

- UHCF fractures occur in nitinol and endurance limits should not be assumed. An observation of no fractures beyond 10^5 cycles when testing to 10 or 100 million cycles is not evidence there will be no fractures at higher numbers of cycles.

- FEA simulations of the full rotary bend test setup predict local variation in peak alternating strains along the length of the wire specimens and some asymmetric biases of the absolute maximum alternating strain that, qualitatively, agree well with fracture locations observed in the experimental fatigue results. With cyclic phase transformation, regions of high cyclic strain concentrate, and fractures usually occur before 10^5 cycles. Without cyclic phase transformation, fatigue life may increase to the UHCF domain.

- Inclusions generate fatigue fractures based on the dimension transverse to the stress load.

- Murakami's relation for the safe stress based on hardness and fracture site inclusion sizes modeled the distribution of UHCF fractures well considering that we made no adjustments to account for differences between high-strength steel and nitinol. The Murakami methodology may provide a path to estimate nitinol fatigue life from metallurgical and material property data.

- Standard metallographic analysis of the inclusion sizes and the use of extreme value statistics provided a good estimate of the mean size of the crack initiating inclusions in both LCF and UHCF. K_{th} calculations based on the fully reversed load stain amplitude and the fracture site inclusion Sqrt(area) of 19 of 20 fractures at greater than 10^7 cycles suggest, using Murakami's damage model, that sub-threshold Ks in the range of 1.1 to 1.6 MPa m$^{1/2}$ grow during 100's of millions of cycles until reaching a $K_{threshold}$ of about 2.3 MPa m$^{1/2}$ at which point cracks quickly propagate to fracture.

- Though a good fit of ε–N data can be developed using the standard Coffin-Manson equation, a two-mode model provides a better fit when the model is assessed using the cumulative distributions. Specifically, a two-mode model is required to capture the paucity of data between 10^5 and 10^8 cycles, the "8 to 5 gap," and will provide more insight when used for experimental test simulation and design.

Supplementary Material

Refer to Web version on PubMed Central for supplementary material.

Acknowledgements

Data Availability

The experimental fatigue life dataset is provided with this published article as a supplementary file. All other datasets are available from the corresponding author on reasonable request.

References

1. Gbur JL, Lewandowski JJ (2016) Fatigue and fracture of wires and cables for biomedical applications. Int Mater Rev 61(4):231–314

2. Mahtabi MJ, Shamsaei N, Mitchell MR (2015) Fatigue of Nitinol: The state-of-the-art and ongoing challenges. J Mech Behav Biomed Mater 50:228–254 [PubMed: 26160028]

3. Pelton A, Berg B, Saffari P, Stebner A, and Bucsek A, Pre-strain and Mean Strain Effects on the Fatigue Behavior of Superelastic Nitinol Medical Devices. Shape Memory and Superelasticity, 2022: p. 1–21.

4. Pelton A, Pelton S, Jörn T, Ulmer J, Niedermaier D, Plaskonka K, LePage W, Saffari P, and Mitchell M The quest for fatigue-resistant nitinol for medical implants. in Fourth symposium on fatigue and fracture of metallic medical materials and devices. 2019. ASTM International.

5. Robertson S, Pelton A, Ritchie R (2012) Mechanical fatigue and fracture of Nitinol. Int Mater Rev 57(1):1–36

6. Fitzka M, Rennhofer H, Catoor D, Reiterer M, Lichtenegger H, Checchia S, di Michiel M, Irrasch D, Gruenewald T, Mayer H (2020) High Speed In Situ Synchrotron Observation of Cyclic Deformation and Phase Transformation of Superelastic Nitinol at Ultrasonic Frequency. Exp Mech 60(3):317–328

7. Adler P, Frei R, Kimiecik M, Briant P, James B, Liu C (2018) Effects of tube processing on the fatigue life of nitinol. Shape Memory and Superelasticity 4(1):197–217

8. Bonsignore C, Shamini A, Duerig T (2019) The Role of Parent Phase Compliance on the Fatigue Lifetime of Ni–Ti. Shape Memory and Superelasticity 5(4):407–414

9. Pelton AR, Fino-Decker J, Vien L, Bonsignore C, Saffari P, Launey M, Mitchell MR (2013) Rotary-bending fatigue characteristics of medical-grade Nitinol wire. J Mech Behav Biomed Mater 27:19–32 [PubMed: 23838356]

10. Robertson SW, Launey M, Shelley O, Ong I, Vien L, Senthilnathan K, Saffari P, Schlegel S, Pelton AR (2015) A statistical approach to understand the role of inclusions on the fatigue resistance of superelastic Nitinol wire and tubing. J Mech Behav Biomed Mater 51:119–131 [PubMed: 26241890]

11. Tobushi H, Hachisuka T, Yamada S, Lin PH (1997) Rotating-bending fatigue of a TiNi shape-memory alloy wire. Mech Mater 26(1):35–42

12. Wagner M, Sawaguchi T, Kaustrater G, Hoffken D, Eggeler G (2004) Structural fatigue of pseudoelastic NiTi shape memory wires. Materials Science and Engineering a-Structural Materials Properties Microstructure and Processing 378(1–2):105–109

13. Cheng C, Handbook of vascular motion. 2019.

14. Gupta S, Pelton AR, Weaver JD, Gong XY, Nagaraja S (2015) High compressive pre-strains reduce the bending fatigue life of nitinol wire. J Mech Behav Biomed Mater 44:96–108 [PubMed: 25625888]

15. Patel MM and Gordon RF An investigation of diverse surface finishes on fatigue properties of superelastic Nitinol wire. in SMST-2006 Proceedings of the International Conference on Shape Memory and Superelastic Technologies. 2006. Citeseer.

16. Schaffer JE, Plumley DL (2009) Fatigue performance of nitinol round wire with varying cold work reductions. J Mater Eng Perform 18(5):563–568

17. Urbano M, Cadelli A, Sczerzenie F, Luccarelli P, Beretta S, Coda A (2015) Inclusions Size-based Fatigue Life Prediction Model of NiTi Alloy for Biomedical Applications. Shape Memory and Superelasticity 1(2):240–251

18. Weaver J, Sena G, Falk W, Sivan S (2022) On the influence of test speed and environment in the fatigue life of small diameter nitinol and stainless steel wire. Int J Fatigue 155:106619

19. Cao H, Wu MH, Zhou F, McMeeking RM, Ritchie RO (2020) The influence of mean strain on the high-cycle fatigue of Nitinol with application to medical devices. J Mech Phys Solids 143:104057

20. Rahim M, Frenzel J, Frotscher M, Pfetzing-Micklich J, Steeg-muller R, Wohlschlogel M, Mughrabi H, Eggeler G (2013) Impurity levels and fatigue lives of pseudoelastic NiTi shape memory alloys. Acta Mater 61(10):3667–3686

21. Bathias C (1999) There is no infinite fatigue life in metallic materials. Fatigue & fracture of engineering materials & structures (Print) 22(7):559–565

22. Murakami Y, Takada M, and Toriyama T, Super-long life tension–compression fatigue properties of quenched and tempered 0.46% carbon steel. International Journal of Fatigue, 1998. 20(9): p. 661–667.

23. Murakami Y, Metal fatigue: effects of small defects and non-metallic inclusions. 2019: Academic Press.

24. ASTM F2063–12, Standard Specification for Wrought Nickel-Titanium Shape Memory Alloys for Medical Devices and Surgical Implants, ASTM International.

25. ASTM F2082–16, Standard Test Method for Determination of Transformation Temperature of Nickel-Titanium Shape Memory Alloys by Bend and Free Recovery, ASTM International.

26. ASTM F2516–18, Standard Test Method for Tension Testing of Nickel-Titanium Superelastic Materials, ASTM International.

27. ASTM F2004–17, Standard Test Method for Transformation Temperature of Nickel-Titanium Alloys by Thermal Analysis, ASTM International.

28. ASTM E384–17, Standard Test Method for Microindentation Hardness of Materials, ASTM International.

29. ASTM E3–11, Standard Guide for Preparation of Metallographic Specimens, ASTM International.

30. ASTM E407–07, Standard Practice for Microetching Metals and Alloys, ASTM International.

31. ASTM E2283–08, Standard Practice for Extreme Value Analysis of Nonmetallic Inclusions in Steel and Other Microstructural Features, ASTM International.

32. Schneider CA, Rasband WS, Eliceiri KW (2012) NIH Image to ImageJ: 25 years of image analysis. Nat Methods 9(7):671–675 [PubMed: 22930834]

33. Aycock KI, Rebelo N, Craven BA (2020) Method of manufactured solutions code verification of elastostatic solid mechanics problems in a commercial finite element solver. Comput Struct 229:106175

34. Rebelo N, Perry M (2000) Finite element analysis for the design of nitinol medical devices. Minim Invasive Ther Allied Technol 9(2):75–80

35. Auricchio F, Taylor RL (1997) Shape-memory alloys: modelling and numerical simulations of the finite-strain superelastic behavior. Comput Methods Appl Mech Eng 143(1–2):175–194

36. Pedregosa F, Varoquaux G, Gramfort A, Michel V, Thirion B, Grisel O, Blondel M, Prettenhofer P, Weiss R, and Dubourg V, Scikit-learn: Machine learning in Python. the Journal of machine Learning research, 2011. 12: p. 2825–2830.

37. Marrey R, Baillargeon B, Dreher ML, Weaver JD, Nagaraja S, Rebelo N, and Gong X-Y, Validating Fatigue safety factor calculation methods for cardiovascular stents. Journal of biomechanical engineering, 2018. 140(6).

38. Craven BA, Aycock KI, Manning KB (2018) Steady flow in a patient-averaged inferior vena cava—Part II: Computational fluid dynamics verification and validation. Cardiovasc Eng Technol 9(4):654–673 [PubMed: 30446978]

39. Roache PJ (1994) Perspective: A Method for Uniform Reporting of Grid Refinement Studies. J Fluids Eng 116(3):405–413

40. Guler I, Aycock K, and Rebelo N, Two Calculation Verification Metrics used in the Medical Device Industry: Revisiting the Limitations of Fractional Change. The Journal of Verification, Validation, and Uncertainty Quantification (JVVUQ), 2022 (Accepted).

41. Pelton A, Huang G, Moine P, Sinclair R (2012) Effects of thermal cycling on microstructure and properties in Nitinol. Mater Sci Eng, A 532:130–138

42. Castillo E and Fernández-Canteli A, A unified statistical methodology for modeling fatigue damage. 2009: Springer Science & Business Media.

43. Meeker WQ, E.L., Pascual FG, Hong Y, Falk WM, Ananthasayanam B, Liu P, Modern Statistical Models and Methods for Estimating Fatigue-Life and Fatigue-Strength Distributions from Experimental Data. (in preparation).

44. Falk W A Statistically Rigorous Fatigue Strength Analysis Approach Applied to Medical Devices. in Fourth Symposium on Fatigue and Fracture of Metallic Medical Materials and Devices. 2019. ASTM International.

45. Sakai T, Lian B, Takeda M, Shiozawa K, Oguma N, Ochi Y, Nakajima M, Nakamura T (2010) Statistical duplex S-N characteristics of high carbon chromium bearing steel in rotating bending in very high cycle regime. Int J Fatigue 32(3):497–504

46. Chandran KR, Chang P, Cashman G (2010) Competing failure modes and complex S-N curves in fatigue of structural materials. Int J Fatigue 32(3):482–491

47. Chan V, Meeker WQ (1999) A failure-time model for infant-mortality and wearout failure modes. IEEE Trans Reliab 48(4):377–387

48. Paolino D, Tridello A, Chiandussi G, Rossetto M (2015) Statistical distributions of Transition Fatigue Strength and Transition Fatigue Life in duplex S-N fatigue curves. Theoret Appl Fract Mech 80:31–39

49. Murakami Y, Beretta S (1999) Small defects and inhomogeneities in fatigue strength: experiments, models and statistical implications. Extremes 2(2):123–147

50. Roiko A, Murakami Y (2012) A design approach for components in ultralong fatigue life with step loading. Int J Fatigue 41:140–149

51. Yamashita Y, Murakami Y (2016) Small crack growth model from low to very high cycle fatigue regime for internal fatigue failure of high strength steel. Int J Fatigue 93:406–414

52. Murakami Y, Nomoto T, Ueda T, and Murakami Y, On the mechanism of fatigue failure in the superlong life regime ($N\rangle 107$ cycles). Part 1: influence of hydrogen trapped by inclusions. Fatigue & Fracture of Engineering Materials & Structures, 2000. 23(11): p. 893–902.

53. ASTM E674–12, Standard Specification for Industrial Perforated Plate and Screens (Round Opening Series), ASTM International.

54. McKelvey A, Ritchie R (2001) Fatigue-crack growth behavior in the superelastic and shape-memory alloy Nitinol. Metall and Mater Trans A 32(3):731–743

55. Robertson S, Ritchie R (2007) In vitro fatigue-crack growth and fracture toughness behavior of thin-walled superelastic Nitinol tube for endovascular stents: A basis for defining the effect of crack-like defects. Biomaterials 28(4):700–709 [PubMed: 17034845]

56. Schijve J, Fatigue of Structures and Materials. 2001: Springer Dordrecht. 520.

57. Racek J, Stora M,Šittner P, Heller L, Kope ek J, Petrenec M (2015) Monitoring tensile fatigue of superelastic NiTi wire in liquids by electrochemical potential. Shape Memory and Superelasticity 1(2):204–230

58. Sun F, Jordan L, Albin V.r., Lair V, Ringuedé A, and Prima F.d.r., On the high sensitivity of corrosion resistance of NiTi stents with respect to inclusions: an experimental evidence. ACS omega, 2020. 5(6): p. 3073–3079. [PubMed: 32095730]

59. ASTM E2948–16A, Standard Test Method for Conducting Rotating Bending Fatigue Tests of Solid Round Fine Wire, ASTM International.

60. Pelton A (2011) Nitinol fatigue: a review of microstructures and mechanisms. J Mater Eng Perform 20(4):613–617

61. Aycock KI, Weaver JD, Paranjape HM, Senthilnathan K, Bonsignore C, Craven BA (2021) Full-field microscale strain measurements of a nitinol medical device using digital image correlation. J Mech Behav Biomed Mater 114:104221 [PubMed: 33309001]

62. Miyazaki S, Mizukoshi K, Ueki T, Sakuma T, and Liu Y, Fatigue life of Ti–50 at.% Ni and Ti–40Ni–10Cu (at.%) shape memory alloy wires. Materials Science and Engineering: A, 1999. 273: p. 658–663.

63. ASTM F3211–17, Standard Guide for Fatigue-to-Fracture (FtF) Methodology for Cardiovascular Medical Devices, ASTM International.
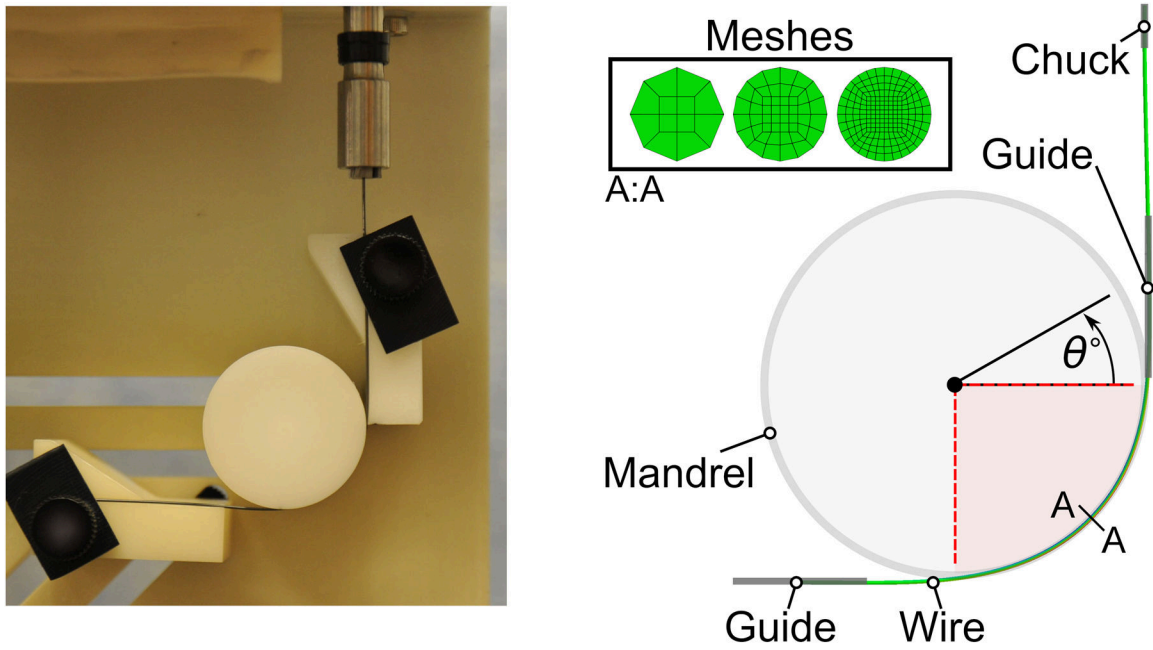
Fig. 1.

(Left) Experimental and (Right) computational setup for rotary bend fatigue testing.

Experimental setup shown without PBS and with mandrel radius of 9.17 mm
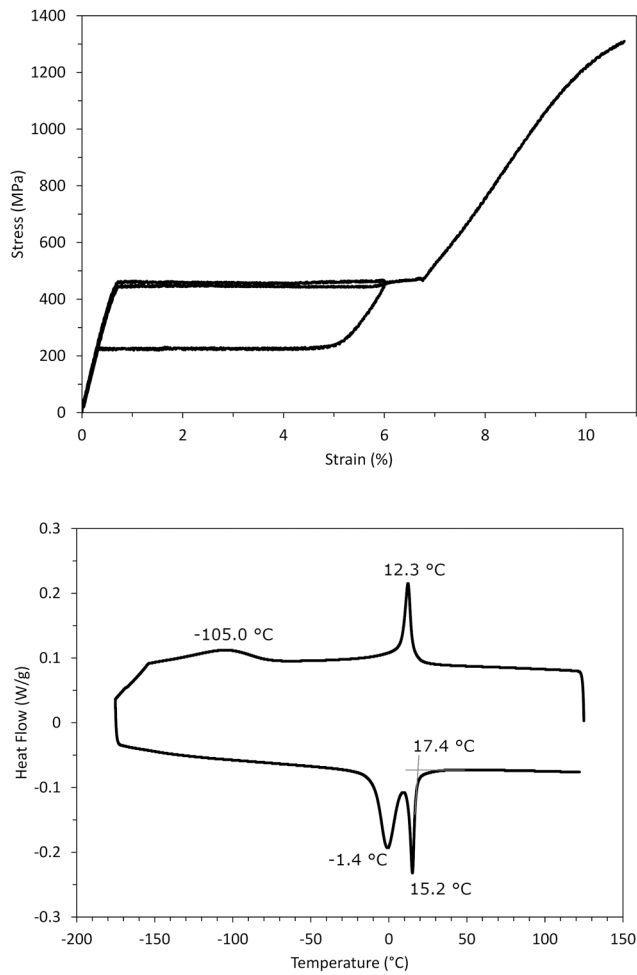
Fig. 2.
Material characterization with engineering stress and strain from tensile testing (top) and differential scanning calorimetry (DSC) curve (bottom) shown with peak temperatures and A_f annotated
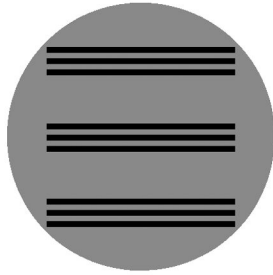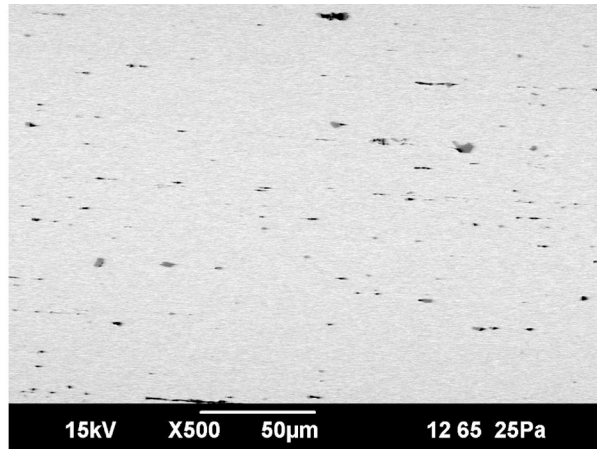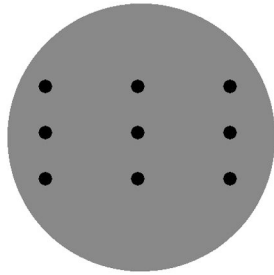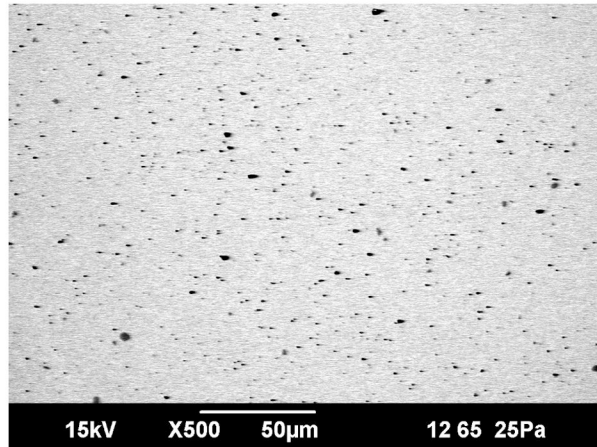
Fig. 3.
Schematic of the metallographic potting for longitudinal (top) and transverse (bottom) specimens and a sample of associated SEM backscatter images. Each metallographic image was 170 μm tall by 254 μm wide
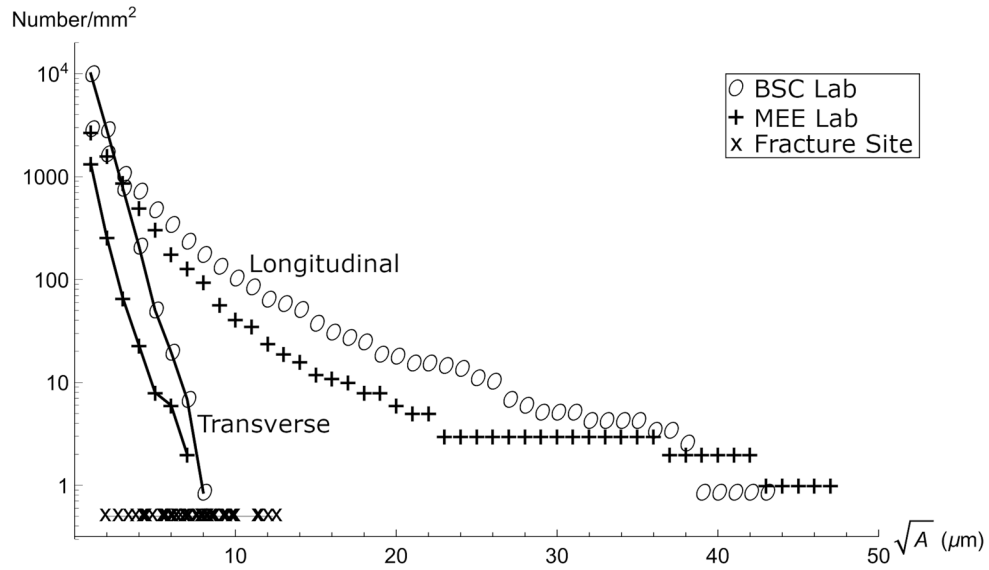
Fig. 4.

Numbers of inclusions per mm^2 for lengths greater than x μm in the total inspected areas of 1.17 mm^2 (BSC) and 1.00 mm^2 (MEE) in the longitudinal (markers only) and transverse (markers and solid line) directions. All data shown are based on the square root area (A) of an ellipse that covered the entire inclusion with the exception of the MEE transverse data. Since MEE only examined longitudinally potted specimens (reference Fig. 3), the MEE transverse data are based on the transverse Feret dimension of longitudinally potted specimens. X markers (arbitrarily placed at 0.5 on the y-axis) show inclusion A measured at fatigue fracture initiation sites. The comparison of the metallographic A to the fracture site makes it clear that the metallographic transverse specimen's A (BSC) or transverse Y-Feret (MEE) on the longitudinal specimens are better predictors than the metallographic longitudinal specimen's A of the fracture surface's fracture initiating inclusion size
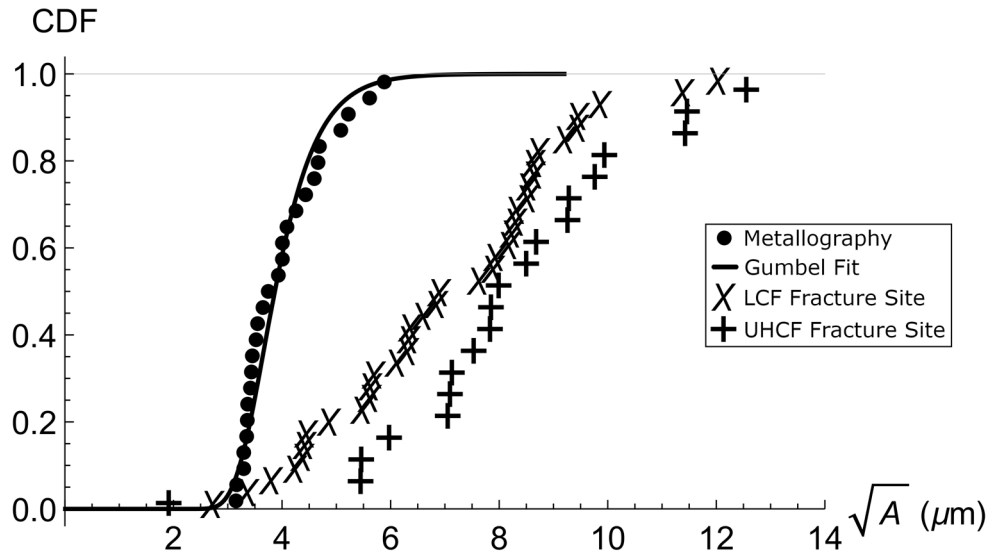
Fig. 5.
Cumulative distribution function (CDF) of inclusion sizes showing the size of the largest inclusions per transverse metallographic image (filled circle) and the corresponding Gumbel extreme value fit (solid line). The actual measured fracture site inclusion sizes for 37 LCF ($N < 10^7$) fractures (times) and 20 UHCF ($N > 10^7$) are also shown (plus). The Gumbel extreme value calculation using the average area at risk of fracture reasonably predicts the average fracture site inclusion size (see "Experimental Rotary Bend Fatigue and Imaging of Fractured Surfaces" section)
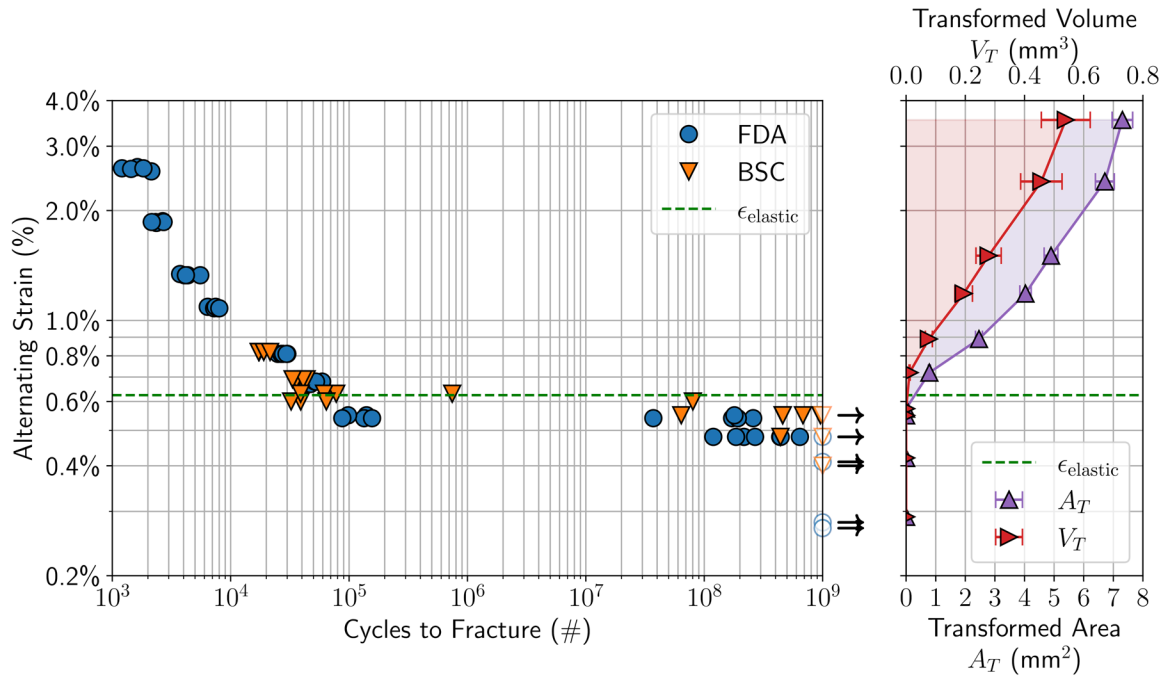
Fig. 6.

Strain-life diagram showing experiments conducted at both laboratories with filled shapes representing fractures and unfilled shapes representing runouts. Experimental alternating strains were calculated for each specimen individually using the engineering estimation in Eq. 3. Corresponding FEA calculations of transformed area A_T and volume V_T per wire rotation versus maximum alternating strain are shown to the right. The dashed horizontal line denotes the maximum elastic strain reached in experimental uniaxial tension testing prior to initiation of the loading plateau region (i.e., $\varepsilon_{elastic} = E/\sigma_{sL}$)
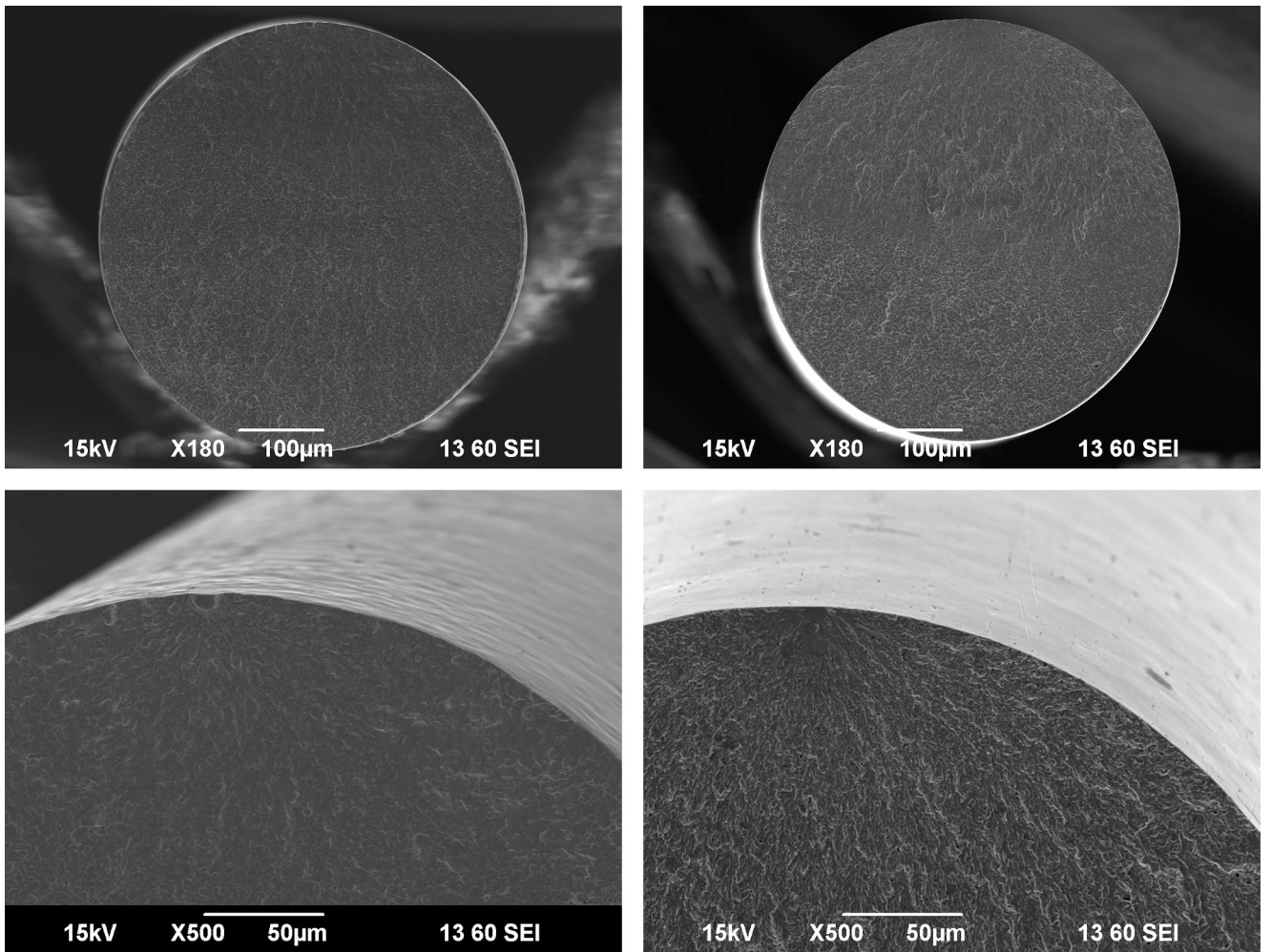
Fig. 7.
Representative SEM images of fracture surfaces. Left: $\varepsilon_a = 1.87\%$ and fracture at 2666 cycles. Right: $\varepsilon_a = 0.48\%$ and fracture at 642,262,481 cycles
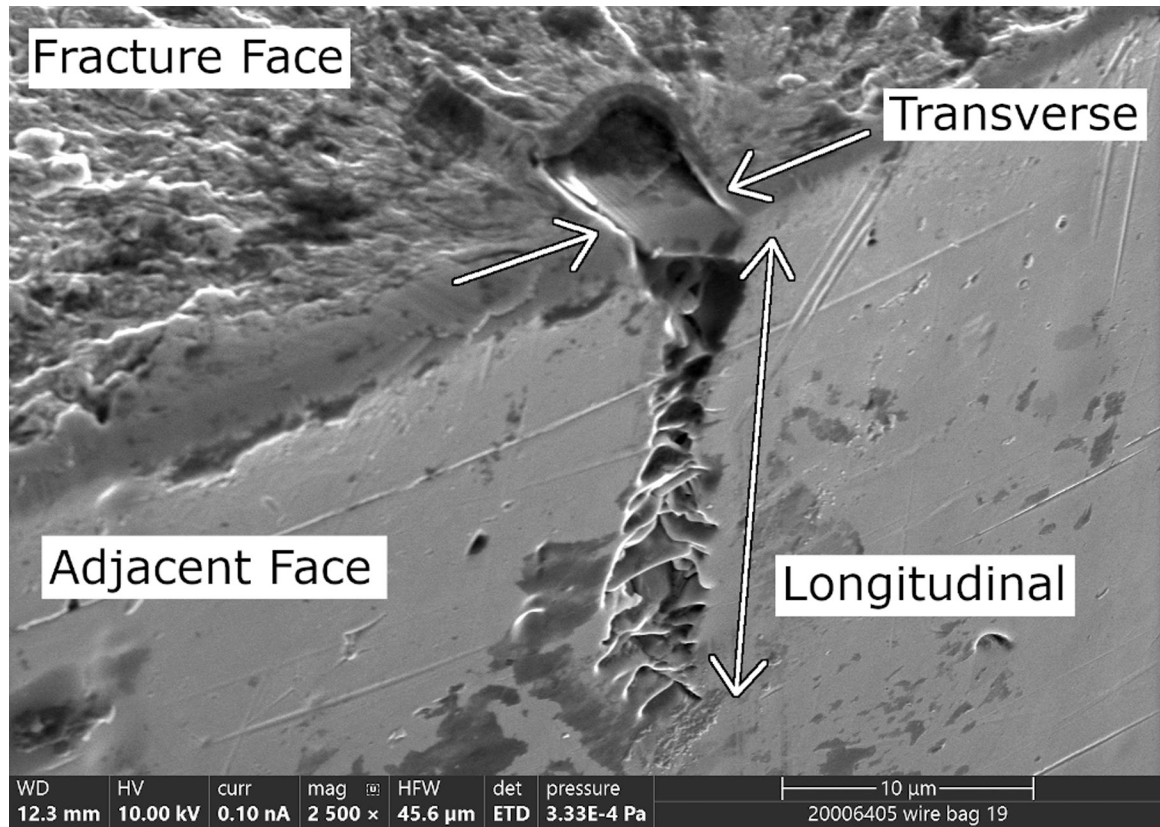
Fig. 8.
SEM image of an UHCF fracture in the region of the inclusion which initiated the fracture.
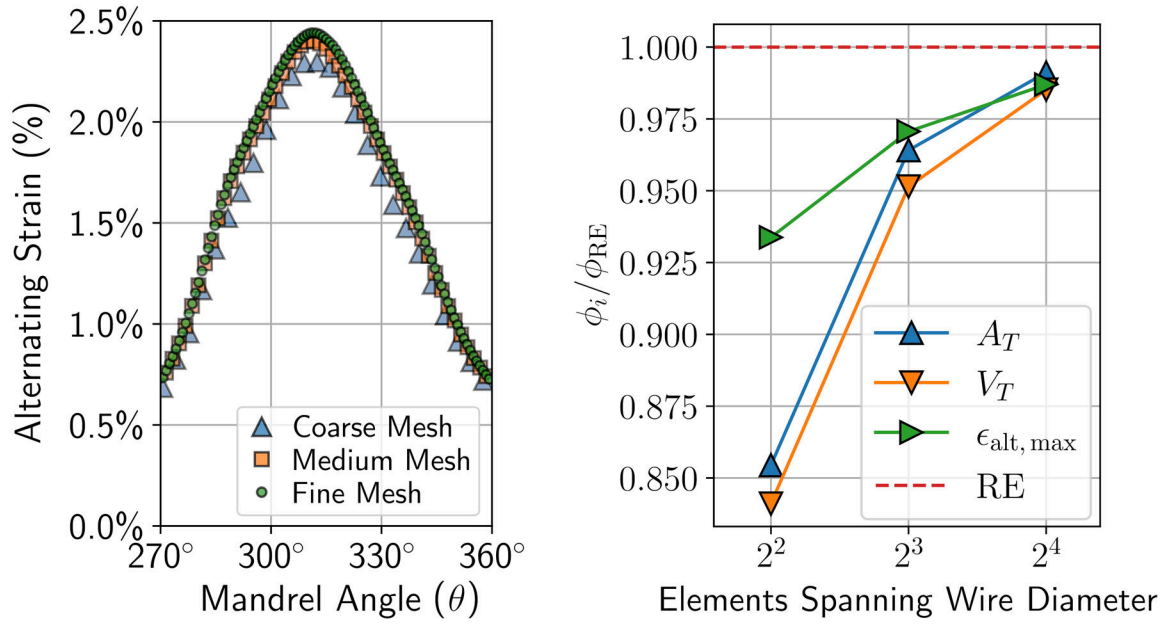The cycle count at fracture for this specimen was 331,876,922

Fig. 9.
Mesh refinement study results. Left) Predicted maximum alternating strain $\varepsilon_{alt;max}$ versus mandrel angle θ (see Fig. 1) for coarse, medium, and fine meshes and Right) predicted quantities of interest φ, normalized by their Richardson extrapolated (RE) values, for the 12.9 mm radius mandrel
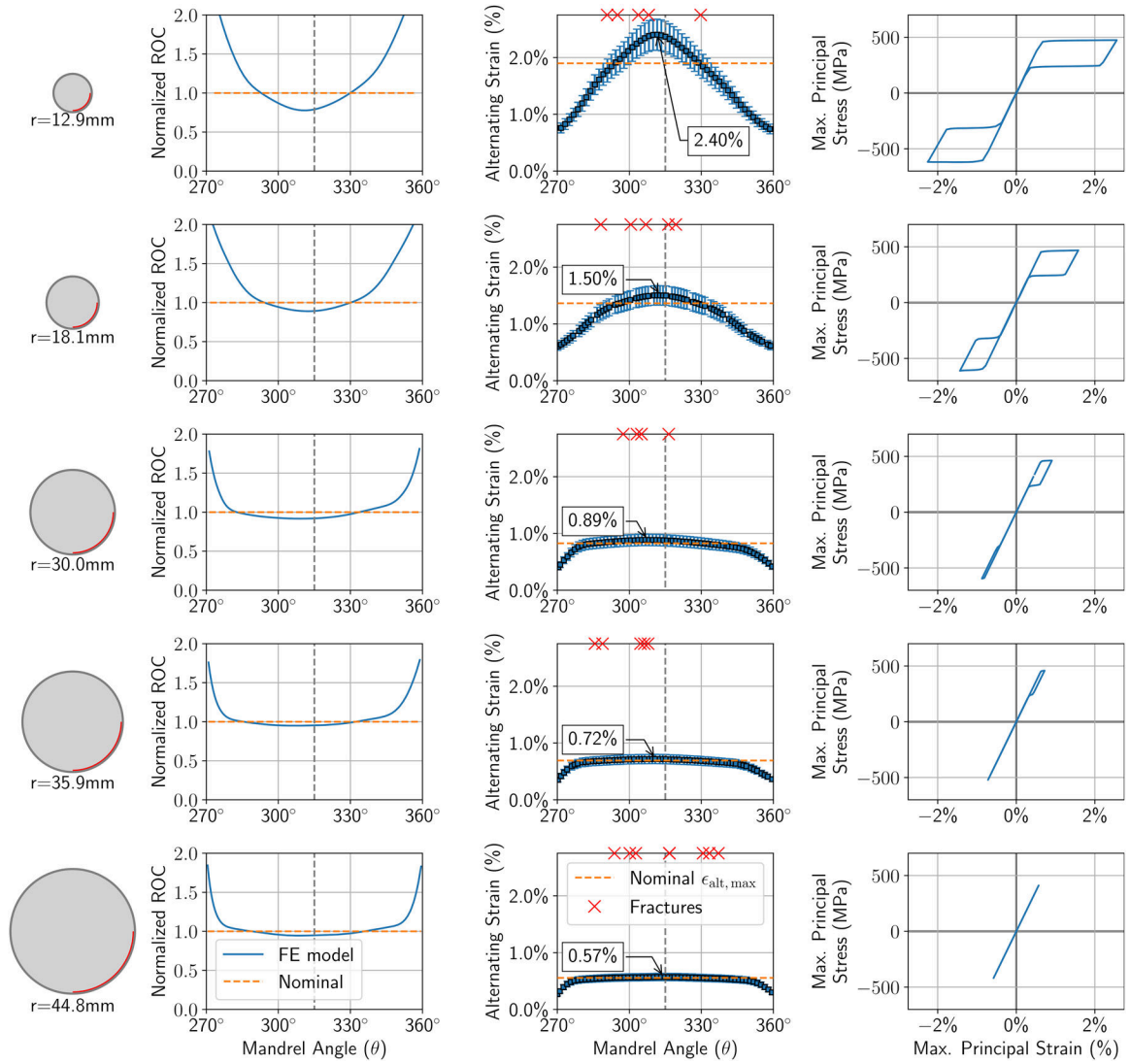
Fig. 10.
From left to right, mandrel size, normalized wire radius of curvature ROC = $r_{local}/(r_{mandrel} + r_{wire})$ versus mandrel angle θ (see Fig. 1), maximum alternating strain $\varepsilon_{alt;max}$ versus mandrel angle θ, and stress–strain curves at integration points associated with the globally maximum alternating strains from FEA simulations. The maximum alternating strain versus mandrel angle also includes experimental data on angular location of fractures which shows the fracture locations correspond approximately to the predicted high strain regions
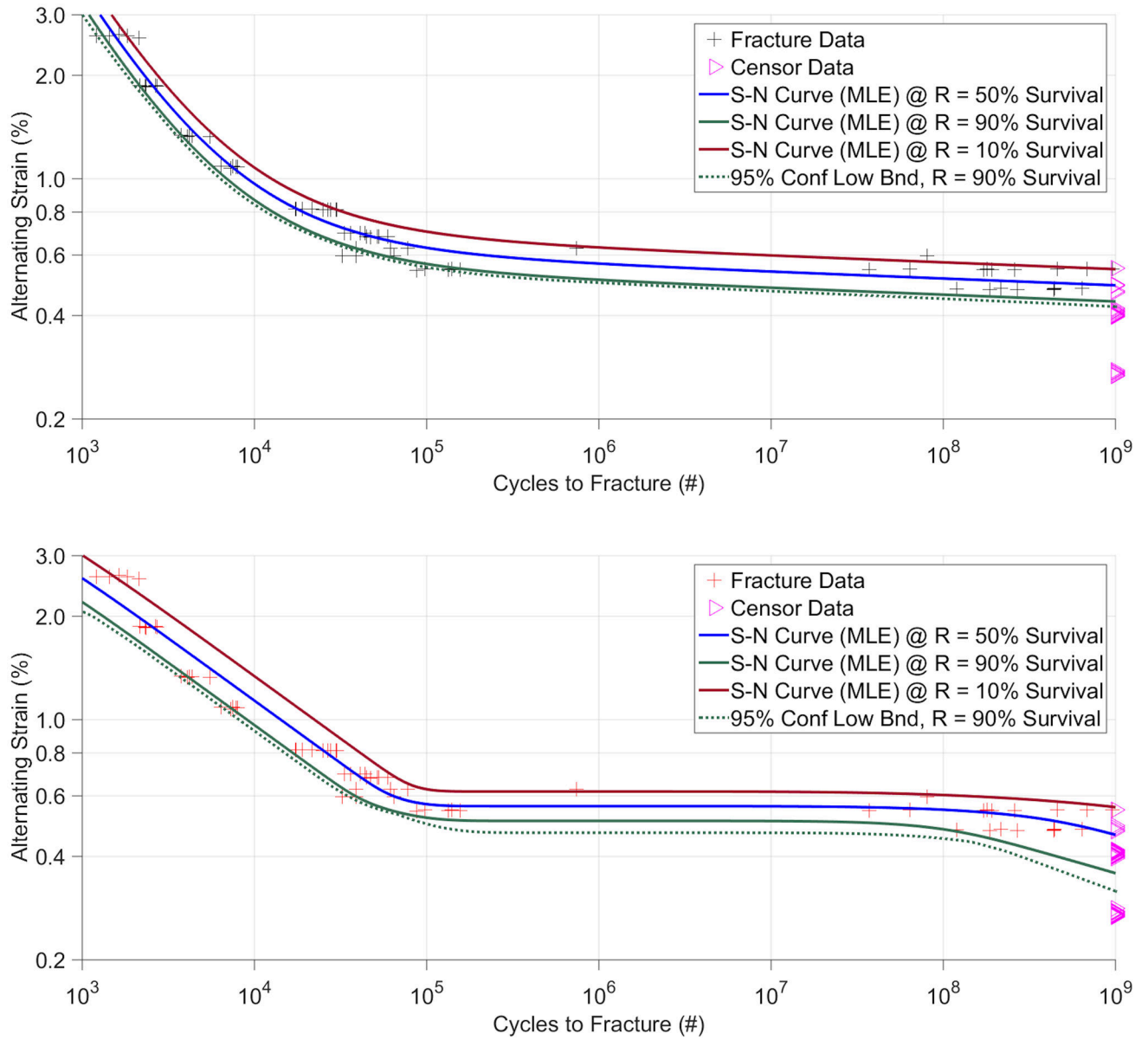
Fig. 11.
Top: Single-failure model fit using the Coffin-Manson Strength Model. Bottom: Two-failure model fit
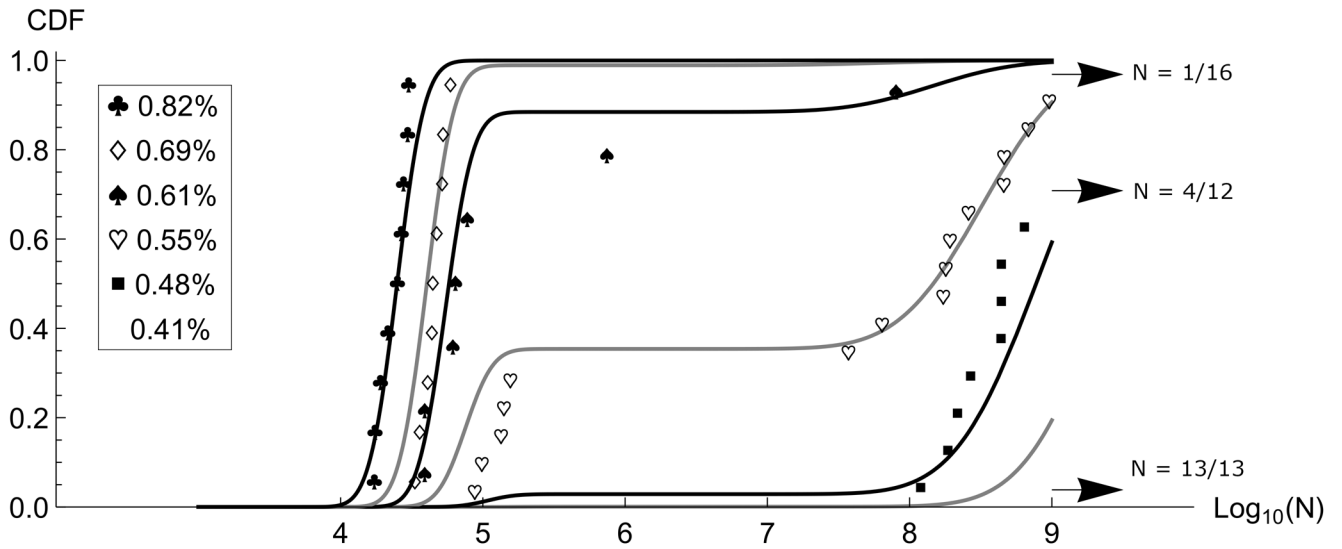
Fig. 12.

CDF of cycles to fracture data and the two-mode model for various alternating strains. For the three lowest alternating strains which all had runouts, an arrow along with the number of runouts over the total number of specimens is shown. Runout arrows are positioned experimentally where the next fracture CDF value would be. For example, because no fractures occurred at 0.41% alternating strain level, there is no marker only an arrow and that arrow is located at 10^9 cycle (runout) and 0.5/13, the CDF of where the 1st fracture would be with 13 specimens
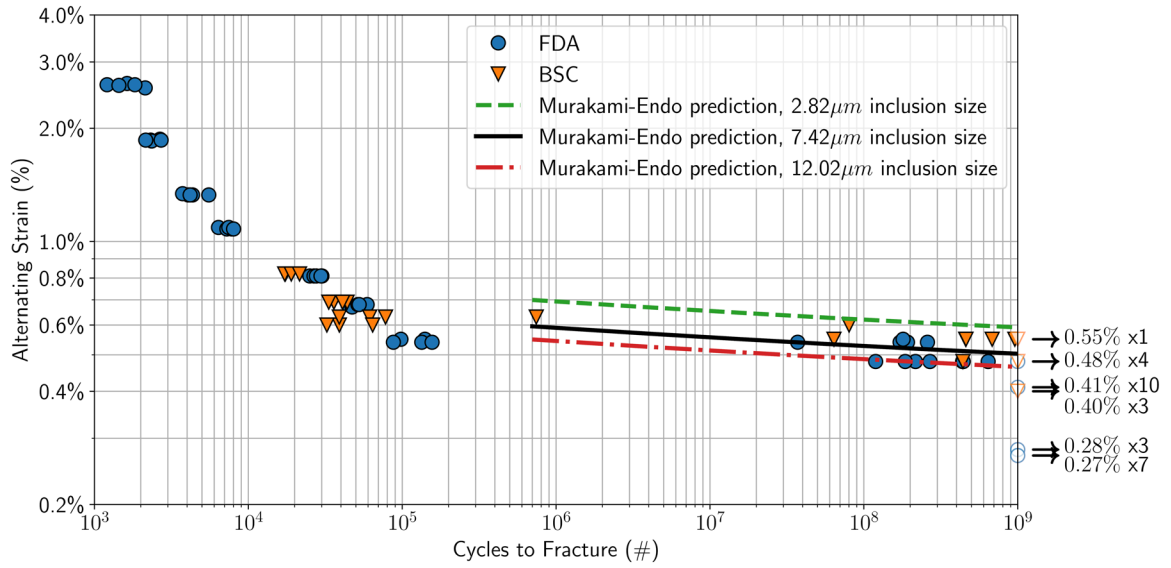
Fig. 13.

The prediction of the safe loading level using the Murakami-Endo model along with damage accumulation (Eq. 28). The black line represents the safe loading level prediction using the average inclusion size (7.42 μm) found at the fatigue fracture initiation site. The green and red lines are calculated with the same method only using the inclusion size that is two standard deviations from the average above (red = 12.02 μm) and below (green = 2.82 μm) the average size

Table 1

FEA material properties

FEA parameter	Value
E_a (MPa)	72,528
E_m (MPa)	28,485
σ_{sL} (MPa)	453
σ_{eL} (MPa)	502
σ_{sU} (MPa)	247
σ_{eU} (MPa)	230
$e_{L;LV}$	0.048
$v_{\{a,m\}}$	0.33

Table 2

Quantities of interest extracted from finite element simulations

Description	Symbol	Source element type	Units
Transformed area per rotation	A_T	M3D4R	mm^2
Transformed volume per rotation	V_T	C3D8I	mm^3
Strain amplitude versus mandrel angle	$\varepsilon_{alt}(\theta)$	M3D4R	mm/mm
Globally maximum scalar alternating strain	$\varepsilon_{alt,\ max}$	M3D4R	mm/mm
Associated mean strain at max alternating strain	$\varepsilon_{mean,\ max}$	M3D4R	mm/mm

Table 3

Nominal alternating strain calculations (engineering strain) and corresponding FEA predictions (true strain) assuming a nominal wire diameter of 0.5 mm

Mandrel number	Mandrel radius, ρ (mm)	Alternating strain, e_a per Eq. 3 (%)	FEA peak predicted alternating strain (%)	FEA peak martensite fraction	FEA corresponding mean strain (%)
I	9.17	2.65	3.54	0.577	0.314
II	12.92	1.90	2.40	0.359	0.189
III	18.09	1.36	1.50	0.179	0.0914
IV	22.41	1.10	1.18	0.113	0.0534
V	29.99	0.83	0.89	0.053	0.0230
VI	35.87	0.69	0.72	0.018	3.87e–03
VII	44.78	0.56	0.57	0	1.86e–03
VIII	50.63	0.49	0.55	0	4.78e–03
IX	59.53	0.42	0.42	0	8.54e–04
X	89.19	0.28	0.29	0	6.93e–04